ISSN: 2630-4503

MATERIALS ENGINEERING RESEARCH

VOLUME 1
ISSUE 1
JANUARY 2019

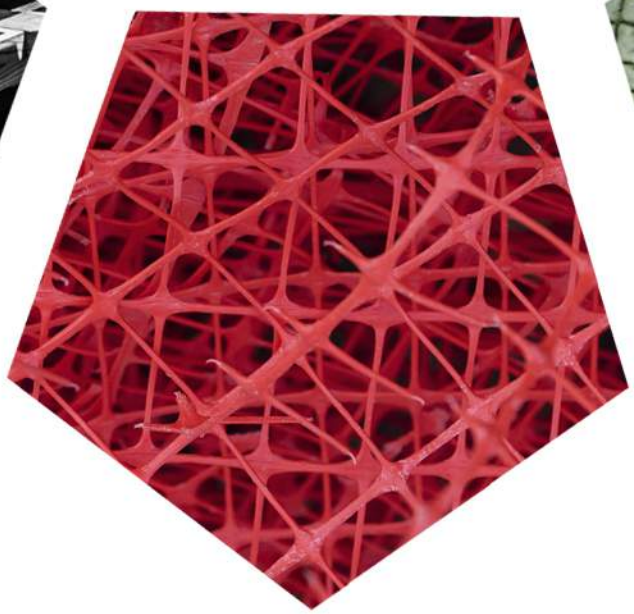

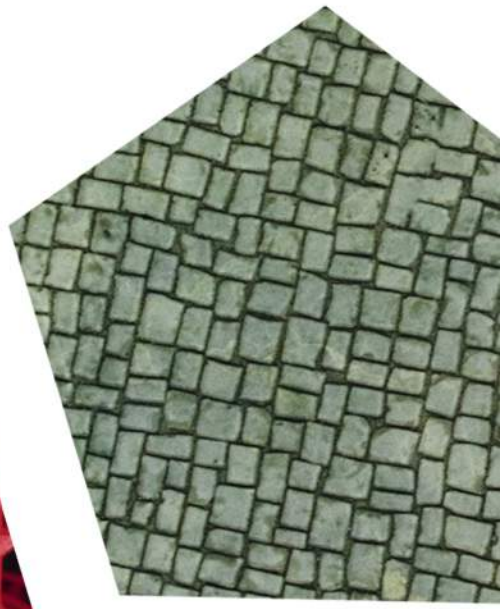

SyncSci PUBLISHING

Editorial Board

Editor-in-Chief

Editorial Board Members

Editorial Board Members

January 2019 | Volum 1 | Issue 1 | Page 1-31
http://www.syncsci.com/journal/index.php/MER

Materials Engineering Research

Contents

RESEARCH ARTICLE

Mater. Eng. Res., 2018, 1(1): 1−6
DOI: 10.25082/MER.2018.01.001

RESEARCH ARTICLE

Chemical stability and thermodynamics of new Zr_2-based heusler alloys

Saleem Yousuf[1*] Dinesh C. Gupta[1]

Abstract: We present the spin polarized calculations on the new Zr_2NiX (X = Al, Ga) alloys. Band structure analysis present them as half-metallic compounds with integral spin magnetic moment of 3 B following the general Slater-Pauling rule. Thermal effects on some macroscopic properties using quasi-harmonic Debye model which considers the phononic effects, the effects of pressure and temperature are taken into account. The variations of the thermal expansion coefficient, Debye temperature, Gruneisen parameter γ and heat capacity for the compounds have been investigated for the first time. These thermodynamic properties may prove as a reference for their synthesis.

Keywords: density functional theory, transition-metal compounds, thermodynamics

1 Introduction

The history of the Heusler alloys began in 1903. Friedrich Heusler discovered Cu_2MnAl to be ferromagnetic, although its elements are all non-ferromagnetic.[1] The search initiated for other Heusler alloys with similar unit cells, only after when in 1929, scientists understood the microstructure completely. The theoretical prediction of 100% spin polarization of some Heusler alloys[2] especially Co_2MnSi[3] makes them interesting for spin-electronic applications as an alternative for conventional 3*d* Ferro-magnets, such as Fe, Co or Ni and their alloys, exhibiting only 51% spin polarization at low temperatures.[4] The two Co sub-lattices are positioned at (0, 0, 0) and (1/2, 1/2, 1/2), where the Mn sub-lattice is at (1/4, 1/4, 1/4) and the Sb sub-lattice at (3/4, 3/4, 3/4) in the unit cell. Thus, eight cobalt atoms surround silicon and manganese atoms. Each cobalt atom has four silicon and four manganese atoms as next neighbors.

In present scenario efforts are focussed on the search of the new materials mainly focussed to use for spin technology to fulfil the basic demands of present technological era such as the powerful new generation of computing devices, shape memory devices etc.[5–7] Spintronics and magneto electronics which are the backbone in these fields desire for the search of novel material which possibly will revolutionise these fields.[8,9] The advancement in spintronic devices have proven from the efficient and desirable 100% spin-polarized currents obtained at the Fermi level. These properties are proven by the eminent materials like half metallic materials that have electrons of unique spin polarization, around the Fermi level.[10–14] They are proving to be the promising candidate for use as spin injectors.[15]

The Zirconium based Heusler alloys have rarely been studied so far and hence, the present study is aimed to investigate the electronic structure, magnetism and transport properties of Zr_2NiX Heusler compounds. The less toxic nature of zirconium has attracted the search of novel spintronic materials with unusual properties at the room temperature.

2 Computational methods

The calculations were carried out using the First-principles full-potential linearized augmented plane wave method (FP-LAPW).[16] The generalised gradient approximation (GGA)[17] is taken for the exchange-correlation potential. Inside the non-overlapping spheres of muffin-tin radius (R_{MT}), the linear combination of radial solution of the Schrdinger equation times the spherical harmonics is used, whereas the plane basis set is chosen in the interstitial region. The muffin tin radii for Zr, Ni were set to 2.3 a.u. and 2.35 a.u., respectively while as 1.8 a.u and 1.9 a.u for Al and Ga, respectively. R_{MT} is chosen in such a way that there is no charge leakage from the core and the total energy convergence is ensured. Further, for the energy Eigen-value convergence, the wave function in the interstitial region is ex-

Received: March 26, 2018; **Accepted:** April 20, 2018; **Published:** April 28, 2018

*Correspondence to: Saleem Yousuf, Condensed Matter Theory Group, School of Studies in Physics, Jiwaji University, Gwalior 474011, India; Email: nengroos-aleem17@gmail.com

[1] Condensed Matter Theory Group, School of Studies in Physics, Jiwaji University, Gwalior 474011, India.

Citation: Yousuf S and Gupta DC. Chemical stability and thermodynamics of new Zr_2-based heusler alloys. *Mater Eng Res*, 2018, **1**(1):1−6

panded in terms of plane waves with a cut-off parameter $K_{MAX}R_{MT}$ = 9.00. The maximum value of the angular momentum l_{MAX} =10 is taken for the wave function expansion inside the atomic spheres. In the interstitial region the charge density and the potential were expanded as a Fourier series with the wave vector up to G_{MAX} =12 a.u^{-1}. The $k-$integration mesh was set to a size of (17×17×17) during the self-consistent cycles and a doubled k- mesh for calculation of the density of states. The self-consistent calculations are considered to converge only when the calculated total energy of the crystal converges to less than 10^{-4} Ry.

In order to study thermal effects, quasi-harmonic Debye model. The model is sufficiently flexible in giving all thermo-dynamical quantities by incorporating the obtained results of energy and volume. In this model, non-equilibrium Gibbs function G*(V; P, T) is defined as follows

$$G^*(V;P,T) = E(V) + PV + A_{vib}(\theta(V),T) \quad (1)$$

where E(V) represents the total energy/formula unit, PV is the constant hydrostatic pressure condition, θ(V), is the Debye temperature and A_{vib} is the lattice vibration expressed as

$$A_{vib}(\theta,T) = nk_BT\left[\frac{9\theta}{8T} + 3ln(1-e^{\frac{\theta}{T}}) - D(\theta/T)\right] \quad (2)$$

where n represents the number of atoms/formula unit, D(θ/T) reperesents the Debye integral, where for the anisotropic solid, θ is expressed by the following expression:

$$\theta = \frac{h}{k}\left[6\pi^2V^{1/2}n\right]^{1/3} f(\nu)\sqrt{\frac{B_s}{M}} \quad (3)$$

here M is the molecular mass, and B_s the adiabatic bulk modulus, and f(ν) is defined as

$$f(\nu) = \left\{3\left[2\left(\frac{21+\sigma}{31-2\sigma}\right)^{3/2} + \left(\frac{11+\sigma}{31-\sigma}\right)^{3/2}\right]^{-1}\right\}^{1/3} \quad (4)$$

And σ is the Poisson ratio in the above relation. In order to get minimized value of the non-equilibrium Gibb's function with respect to volume at constant pressure and temperature mathematically is obtained as

$$\left(\frac{\partial G^*(V;P,T)}{\partial V}\right)_{P,T} = 0 \quad (5)$$

After solving above equation, one can obtain a relation for V(P,T), i.e., thermal equation of state (EOS). Using Eq. (5) for different thermal properties, i.e., isothermal bulk modulus (B_T), specific heat capacity values at constant volume (C_V) and at constant pressure (C_P) and thermal expansion coefficient can be evaluated using the following formulas:

$$B_T(P,T) = V\left(\frac{\partial^2 G^*(V;P,T)}{\partial V^2}\right) \quad (6)$$

$$C_V = 3nk_B\left[4D\left(\theta/T\right) - \frac{3\theta/T}{e^{\theta/T}-1}\right] \quad (7)$$

$$C_P = C_V(1+\alpha\gamma T) \quad (8)$$

$$\alpha = \frac{\gamma C_V}{B_T V} \quad (9)$$

Where γ is the Gruneisen parameter and is calculated from the following expression:

$$\gamma = -\frac{dln\theta(V)}{dlnV} \quad (10)$$

3 Results and discussion

3.1 Structural properties and chemical stability

Highly magnetic materials mainly having either the $L2_1$ and or $C1_b$[18] crystallographic phases have been of interest for both theorists and experimentalists since their discovery. The interest is mainly focused due to their strong ferromagnetic character, subsequently their usage as the testing grounds for the development of new magnetic systems. These novel class families share simultaneously the property of an energy gap between valence and conduction bands for electrons of one spin polarization and the property of continuous band for other spin polarization. This asymmetric character reflects the character of $L2_1$ structure itself. In general, experimental preparation and interpretation of true half-metallic compounds are still scarce, therefore from the beginning, structural optimization is needed to estimate the magnetically and structurally stable phase by means of the total energy minimization. In the present series of new Zr_2NiX (Z=Al, Ga) alloys we have investigated the stable ground state phase among the structures possible. Mostly the zirconium based Heusler alloys crystallize in the cubic ordered Full-Heusler ($L2_1$) structure of Hg2CuTi-type, with space group F-43m at ambient conditions. For the present compounds, Hg_2CuTi (space group 216) is found to be the stable ground state as shown in Figure 1.

Firstly, in order to assure their chemical stability and existence, we have calculated the formation energy of these alloys defined by the following equation:

$$E_f = E_{Zr_2NiZ} - 2E_{Zr} - E_{Ni} - E_Z \quad (11)$$

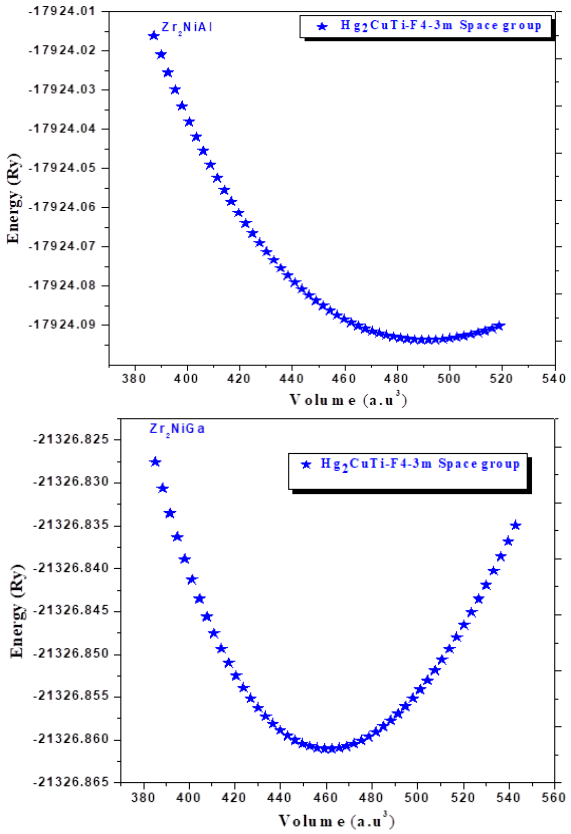

Figure 1. Calculated total energy as a function of unit cell volume of Zr_2NiAl and Zr_2NiGa in Hg_2CuTi-type structures with F4-3m space group

where E_{Zr_2NiZ} are the calculated equilibrium total energies of alloys per formula unit, E_{Zr}, E_{Ni} and E_Z are the chemical potential of these atoms in their stable bulk phases. Results showed that the $E_{formation}$ of the Zr_2NiZ (Z= Al, Ga) alloys are -2.33 eV, -2.63 eV, respectively. The calculated formation energy turns out to be negative and comparable for the same kind of compounds.[19] Negative formation energy indicates that the alloys are thermodynamically stable. In addition, we also calculate the cohesive energy to evaluate the strength of bonding of studied alloys. The cohesive energy is obtained from the following relation:[20]

$$E_{coh} = 2E_{atom}^{Zr} + E_{atom}^{Ni} + E_{atom}^{Z} + E_{total}^{Zr_2NiZ} \quad (12)$$

where $E_{total}^{Zr_2NiZ}$ is the total energies of alloys at equilibrium per formula unit, and E_{atom}^{Zr}, E_{atom}^{Ni}, E_{atom}^{Z} are the total energies of the pure atomic components. It is evident that the cohesive energy is the energy required to break the crystal into isolated atoms, which is not only an indicator of the bonds strength but also an indicator of the mobility of atoms in crystal. In Figure 2, we show the cohesive energy of alloys, it is observed that Zr_2NiAl has the strongest bonding in comparison to the Zr_2NiGa due to its larger cohesive energy, implying that it is difficult to deform in comparison to the latter.

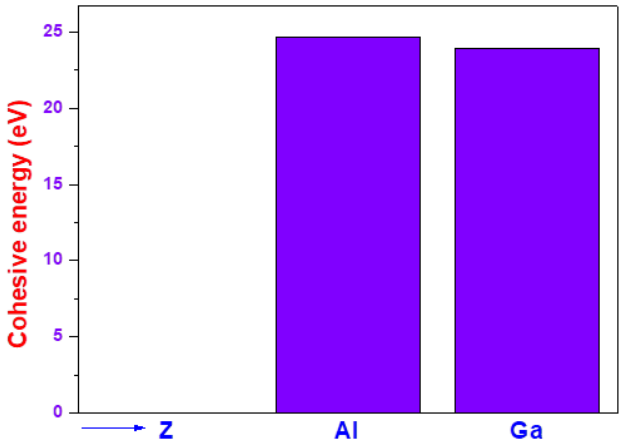

Figure 2. The calculated cohesive energy is presented for Zr_2NiZ alloys with respect to atomic no. (Z)

3.2 Magnetic Properties

Magnetic materials are now-a-days regarded as the potential candidates for spintronics. Mostly in case of Heusler alloys, the Y sites contributes greater to the total magnetic moment in comparison to the atoms at X site. In case of Heusler alloys the total magnetic moment is characterized by their total valence electron count defined through the Slater-Pauling rule. Here in our group of compounds the total valence electron count is 21. They satisfy the Z_T-18 rule,[21,22] according to which they present a magnetic moment of $3_{\mu B}$ per unit cell. The total magnetic moment with contributions from various components is given in Table 1. The magnetic alignment is ferromagnetic with maximum contribution from Z_r atoms per unit cell in both compounds. Further it is the different occupation of the *d*-bands for the majority and minority spins that leads to the magnetization in these compounds.

Table 1. The total and atomic magnetic moments of Zr_2NiAl and Zr_2NiGa Compounds where M_{Int} (μB): magnetic moment in the interstitial region and Mtot (μ B) is total magnetic moment.

Compound	$M_{Zr(a)}$	$M_{Zr(b)}$	M_{Ni}	$M_{(Z=Al,Ga)}$	$M_{Int.}$	M_{tot}
Zr_2NiAl	1.02	0.98	0.61	0.15	0.11	2.87
Zr_2NiGa	1.06	0.81	0.58	0.21	0.20	2.86

3.3 Thermodynamic properties

In order to calculate the pressure and temperature dependence of the thermodynamic properties, we

used quasi-harmonic (QH) approximation.[23,24] Specialty is that the values of thermodynamic parameters are computed at the level of the quasi-harmonic Debye model[25,26] approach for full-Heusler Zr_2NiAl and Zr_2NiGa alloys. Several properties are calculated which include the specific heats at constant volume (C_V) and constant pressure (C_P), Debye temperature (θ_D), thermal expansion coefficient (α), and Gruneisen parameter (γ) in temperature range of 0 K to 800 K in steps of 100 K and at pressure ranging from 0 GPa to 70 GPa (Zr_2NiAl) and 0 GPa to 30 GPa (Zr_2NiGa) in steps of 5 GPa.

The graphical variations of various properties are shown in Figure 3, 4 (a, b), our calculated results for C_V and C_P each as a function of temperature are illustrated for Zr_2NiAl and Zr_2NiGa respectively. The important thermodynamic property viz, specific heat capacity is strictly related to the temperature dependence of ultimate thermodynamic functions, and it is utmost central constraint for associating thermodynamics with dynamics and microscopic structure. From the graphical variation, we can see that when the temperature is below 650 K, C_V and C_P variations are very close together demonstrating strong dependence on temperature owing to the anharmonic approximation used in this scheme of calculations. Further, we can also argue that at high temperatures, C_V approaches to a constant value of (97 $Jmol^{-1}K^{-1}$), obeying Dulong and Petit's rule, which is followed by all solids at high temperatures, owing to the suppression of the anharmonic effect.[27] The concluding statement which is quite interesting is that the specific heat capacity at constant pressure C_P increases monotonically with the increase of temperature.

Table 2. Calculated values of Debye temperature θ(K) and Gruneisen parameter (γ) of Zr2NiAl and Zr_2NIGa at various pressures and temperatures

Compound	T (K)	Paramete r	P (GPa) 0	25	50	70
Zr_2NiAl	300	θ	598.24	700.00	779.80	834.09
		γ	1.82	1.63	1.52	1.46
	600	θ	592.84	696.38	776.83	831.51
		γ	1.83	1.63	1.52	1.46
	800	θ	587.98	692.96	774.09	829.09
		γ	1.85	1.64	1.52	1.46
Zr_2NiGa	250	θ	571.82	613.38	651.50	685.77
		γ	1.91	1.83	1.78	1.74
	500	θ	567.48	610.13	648.15	684.69
		γ	1.92	1.84	1.78	1.74
	700	θ	563.53	606.70	645.05	679.83
		γ	1.92	1.85	1.79	1.74

The thermodynamic properties with other physical properties of solids are closely related to the Debye temperature (θ_D) and Gruneisen parameter (γ). The variations of both the properties are respectively shown in Figure 3, 4 (c, d) with their numerical variation enlisted in Table 2. From the analysis of the properties, we can see that Debye temperature increases with increasing pressure whereas the Gruneisen parameter decreases when the temperature is kept constant. Here the concluding statement is that, at constant pressure, the Debye temperature decreases and the Gruneisen parameter increase as the temperature increases.

The mathematical formula reflecting the variation of volume thermal expansion coefficient (α) with volume at constant pressure is given as:

$$\alpha = \frac{1}{V}\left(\frac{\partial V}{\partial T}\right)_P \tag{13}$$

The variation of parameter is shown in Figure 3, 4 (e) with temperature at different pressures for the two compounds. The variation shows that the thermal expansion increases sharply with temperature up to 300 K after then slowly for temperature higher than 300 K, and gradually turns into a linear increase. Furthermore, we can also see that, at a fixed temperature, higher the pressure, smaller the thermal expansion coefficient, indicating that high pressure suppresses thermal expansion. At zero pressure and 300 K, the values of the thermal expansion for Zr_2NiAl and Zr_2NiGA are $1.48\times10^{-5}K^{-1}$ and $1.43\times10^{-5}K^{-1}$, respectively.

4 Conclusion

First principle spin-polarised calculations for new inverse Heusler alloys within the GGA approach show the F4-3m as the ground state of Zr_2NiZ alloys with $L2_1$ ordered structure. Magnetic moment of $3_{\mu B}$ is characterised with the help of generalised Slater-Pauling rule of Z_T-18 rule. Formation energy analysis show that these alloys are chemically stable and can be synthesised experimentally. Finally, the thermodynamic properties including volume variation, heat capacity, Debye temperature, and thermal expansion coefficients of the full-Heusler Zr_2NiAl and Zr_2NiGa compounds are investigated. The observed variations are well according with the results of the Debye theory, which is regularly applied to several materials.

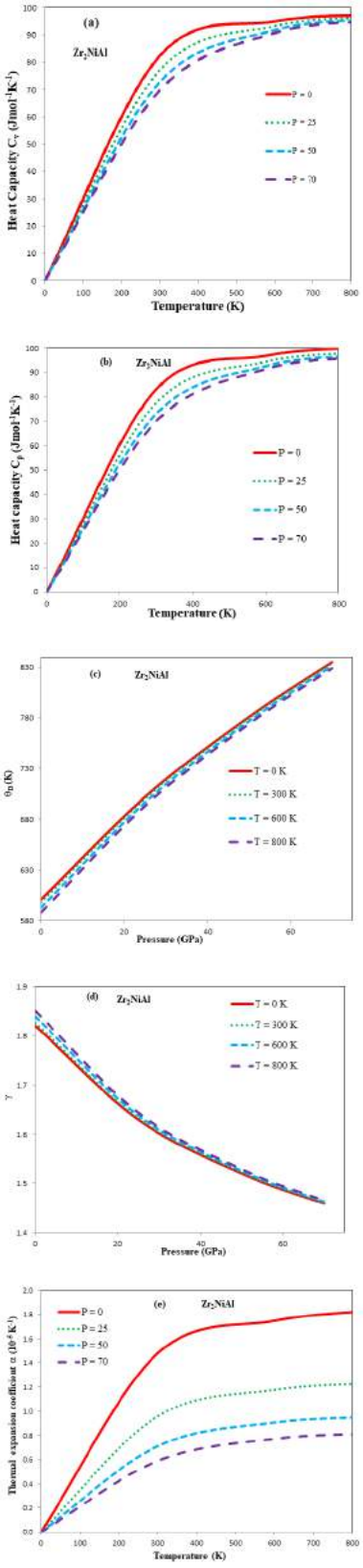

Figure 3. Calculated thermodynamic properties of Zr_2NiAl: (a), (b)−Heat capacity, (c) Debye temperature, (d) Gruneisen parameter, (e) Thermal expansion coefficient.

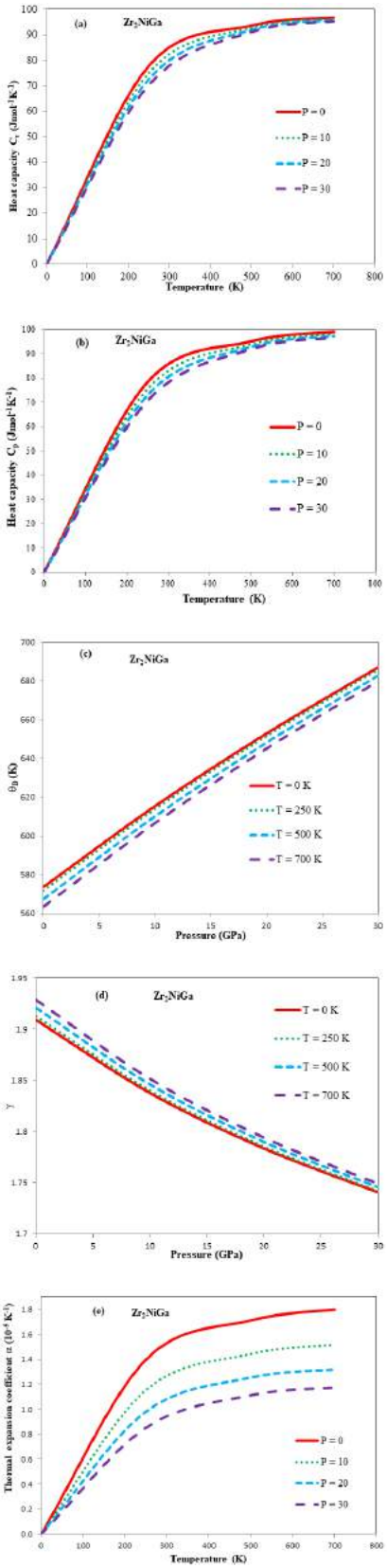

Figure 4. Calculated thermodynamic properties of Zr_2NiGa: (a), (b)−Heat capacity, (c) Debye temperature, (d) Gruneisen parameter, (e) Thermal expansion coefficient.

References

[1] Heusler F. F. Heusler, Verh. Dtsch. Phys. Ges. 5, 219 (1903). *Verh. Dtsch. Phys. Ges.*, 1903, 5: 219.

[2] De Groot RA, Mueller FM, Van Engen PG, *et al*. New class of materials: half-metallic ferromagnets. *Physical Review Letters*, 1983, **50**(25): 2024. https://doi.org/10.1103/PhysRevLett.50.2024

[3] Ishida S, Masaki T, Fujii S, *et al*. Theoretical search for half-metalliic films of Co_2 MnZ (ZSi, Ge). *Physica B: Condensed Matter*, 1998, **245**(1): 1-8. https://doi.org/10.1016/S0921-4526(97)00495-X

[4] Moodera JS, Mathon G. Spin polarized tunneling in ferromagnetic junctions. *Journal of magnetism and magnetic materials*, 1999, **200**(1-3): 248-273. https://doi.org/10.1016/S0304-8853(99)00515-6

[5] Datta S, Das B. Electronic analog of the electro-optic modulator. *Applied Physics Letters*, 1990, **56**(7): 665-667. https://doi.org/10.1063/1.102730

[6] Kilian KA, Victora RH. Electronic structure of $NiCo_2$ MnIn for use in spin injection. *Journal of Applied Physics*, 2000, **87**(9): 7064-7066. https://doi.org/10.1063/1.372932

[7] Tanaka CT, Nowak J, Moodera JS. Spin-polarized tunneling in a half-metallic ferromagnet. *Journal of applied physics*, 1999, **86**(11): 6239-6242. https://doi.org/10.1063/1.371678

[8] Park JH, Vescovo E, Kim HJ, *et al*. Direct evidence for a half-metallic ferromagnet. *Nature*, 1998, **392**(6678): 794. doi:10.1038/33883

[9] Hirohata A, Takanashi K. Future perspectives for spintronic devices. *Journal of Physics D: Applied Physics*, 2014, **47**(19): 193001.

[10] Ishida S, Akazawa S, Kubo Y, *et al*. Band theory of $CoCo_2$ MnSn, $CoCo_2$ TiSn and $CoCo_2$ TiAl. *Journal of Physics F: Metal Physics*, 1982, **12**(6): 1111.

[11] Ishida S, Fujii S, Kashiwagi S, *et al*. Search for half-metallic compounds in $CoCo_2$ MnZ (Z= IIIb, IVb, Vb element). *Journal of the Physical Society of Japan*, 1995,**64**(6): 2152-2157. https://doi.org/10.1143/JPSJ.64.2152

[12] Gupta DC, Bhat IH. Investigation of high spin-polarization, magnetic, electronic and half-metallic properties in $RuMnCo_2Ge$ and $RuMnCo_2Sb$ Heusler alloys. *Materials Science and Engineering: B*, 2015, **193**: 70-75. https://doi.org/10.1016/j.mseb.2014.11.009

[13] Fujii S, Sugimura S, Asano S. Hyperfine fields and electronic structures of the Heusler alloys Co_2 MnX (X= Al, Ga, Si, Ge, Sn). *Journal of Physics: Condensed Matter*, 1990, **2**(43): 8583.

[14] Bhat IH, Yousuf S, Bhat TM, *et al*. Investigation of electronic structure, magnetic and transport properties of half-metallic $MnCo_2$ CuSi and $MnCo_2$ ZnSi Heusler alloys. *Journal of Magnetism and Magnetic Materials*, 2015, **395**: 81-88. https://doi.org/10.1016/j.jmmm.2015.07.022

[15] De Boeck J, Van Roy W, Das J, *et al*. Technology and materials issues in semiconductor-based magnetoelectronics. *Semiconductor Science and Technology*, 2002, **17**(4): 342. https://doi.org/10.1088/0268-1242/17/4/307

[16] Blaha P, Schwarz K, Madsen GKH, *et al*. wien2k. An augmented plane wave+ local orbitals program for calculating crystal properties, 2001.

[17] Schwarz K, Blaha P, Madsen GKH. Electronic structure calculations of solids using the WIEN2k package for material sciences. *Computer Physics Communications*, 2002, **147**(1-2): 71-76. https://doi.org/10.1016/S0010-4655(02)00206-0

[18] Ouardi S, Fecher GH, Felser C, *et al*. Realization of spin gapless semiconductors: the Heusler compound $MnCo_2$ CoAl. *Physical review letters*, 2013, **110**(10): 100401. https://doi.org/10.1103/PhysRevLett.110.100401

[19] Wang XT, Cui YT, Liu XF, *et al*. Electronic structures and magnetism in the $LiCo_2$ AgSb-type Heusler alloys, $ZrCo_2$ CoZ (Z= Al, Ga, In, Si, Ge, Sn, Pb, Sb): A first-principles study. *Journal of Magnetism and Magnetic Materials*, 2015, **394**: 50-59. https://doi.org/10.1016/j.jmmm.2015.06.035

[20] Pugaczowa-Michalska M. Theoretical prediction of ferrimagnetism in $MnCo_2$ FeB, $MnCo_2$ CoB and $MnCo_2$ NiB. *Intermetallics*, 2012, **24**: 128-134. https://doi.org/10.1016/j.intermet.2012.01.004

[21] Slater JC. The ferromagnetism of nickel. *Physical Review*, 1936, **49**(7): 537. https://doi.org/10.1103/PhysRev.49.537

[22] Pauling L. The nature of the interatomic forces in metals. *Physical Review*, 1938, **54**(11): 899. https://doi.org/10.1103/PhysRev.54.899

[23] Otero-de-la-Roza A, Abbasi-Pérez D, Luaña V. Gibbs2: A new version of the quasiharmonic model code. II. Models for solid-state thermodynamics, features and implementation. *Computer Physics Communications*, 2011, **182**(10): 2232-2248. https://doi.org/10.1016/j.cpc.2011.05.009

[24] Blanco MA, Francisco E, Luana V. GIBBS: isothermal-isobaric thermodynamics of solids from energy curves using a quasi-harmonic Debye model. *Computer Physics Communications*, 2004, **158**(1): 57-72. https://doi.org/10.1016/j.comphy.2003.12.001

[25] Marx D, Hutter J. Ab initio molecular dynamics. *Parallel computing*, 2009, **309**(309): 327.

[26] Allen MP, Tildesley DJ. Computer Simulation of Liquids Oxford Univ. Press. 1987.

[27] Peng F, Fu H, Yang X. Ab initio study of phase transition and thermodynamic properties of PtN. *Physica B: Condensed Matter*, 2008, **403**(17): 2851-2855. https://doi.org/10.1016/j.physb.2008.02.022

Mater Eng Res, 2019, 1(1): 7-10
DOI: 10.25082/MER.2019.01.001

RESEARCH ARTICLE

Frumkin-melik-gaykazan model in the potentiodynamic and galvanodynamic regimes of functioning

Rizvan M. Guseynov* Radzhab A. Radzhabov

Abstract: The main purpose of this article is to study the behavior of a metallic electrode in the electrolyte which contains a surface-active substance with the property of adsorbtion-desorbtion, in the galvanodynamic and potentiodynamic rejimes. The study of the electrochemical behavior of a metallic electrode is carried out by operational impedance method, based on the Ohms low on the interaction between the Laplace-transformed expression of current, voltage and complex resistance (impedance). It is obtained the analytical expression of interface voltage-time dependence in a solution which contains a surface-active indifferent substance with the property of adsorbtion-desorbtion; also it is obtained the analytical expression of current density-time dependence which is passing through electrochemical cell in potentiodynamic regime of functioning of the Frumkin-Melik-Gaykazan model. It is established that the relation between the interface metallic electrode-indifferent electrolyte with property of adsorbtion-desorbtion voltage in the galvanodynamic rejime has the character of second order parabola; the relation between current density which is passing through a cell and time in potentiodynamic rejime of functioning in the Frumkin-Melik-Gaykazan model has exponential character.

Keywords: Frumkin Melik Gaykazan model, indifferent electrolyte, adsorbtion-desorbtion, potentiodynamic and galvanodynamic rejimes, current density, interface voltage

1 Introduction

In the case of adsorbtion of the electrochemical indifferent substance in the electrolyte which contains the surface-active component the electrode impedance was examinated by Frumkin and Melik-Gaykazan in the works.[1–3] In the considerated model electrode charge depend on not only the potential but also on amount of the absorbed ions or molecules which charges are interchanges with the metallic surface.

As to as regards faraday process it should be mean that in the appointed region of potentials the surface-active substance do not electrochemically oxidize or reduction on the electrode.[3] The amount of electricity, which is communicated to electrode, it is used up (spend up) on the charging of electric double layer.[1,2] Just (namely) such model of interface electrodeorganic electrolyte solution is obtained the name Frumkin-Melic-Gaykazan model.

The investigation of adsorbtion of organic substances on the metalles of the platinum group is begin intensive in connection with the problem of using organic substances as electrochemical fuel for the combustible elements.[4]

Namely this object (task) was the one of problem of the practical (applied) electrochemistry the basic main purpose of which was the application of the fuel galvanic elements in electro motor car.[1,2]

The equivalent electric circuit of Frumkin and Melik Gaykazan model for the first time was suggestion by Grafov B.M. and Ukshe E.A..[4](see Figure 1).

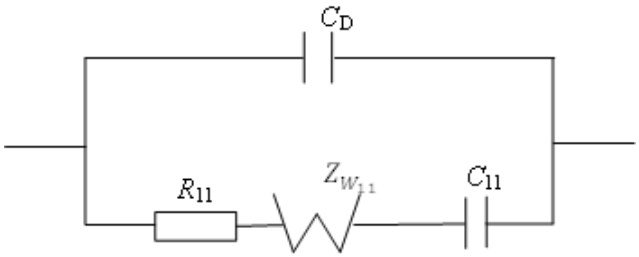

Figure 1. Equivalent electric circuit of Frumkin and Melik-Gaykazan model (scheme)

The structural elements on the Figure 1 are signified: R_{11} and C_{11} are the active resistance and supplementary capacity of the electric double layer which are connected

Received: January 6, 2019; **Accepted:** January 20, 2019; **Published:** January 23, 2019

*Correspondence to: Rizvan M. Guseynov, Dagestan State Pedagogical University, Makhachkala, Russia; Email: rizvanguseynov@mail.ru

Citation: Guseynov RM and Radzhabov RA. Frumkin-melik-gaykazan model in the potentiodynamic and galvanodynamic regimes of functioning. *Mater Eng Res*, 2019, **1**(1): 7-10.

with the adsorption of the surface-active substances in a electrolyte; $Z_{W_{11}}$ is the diffusion impedance of Warburg; CD is the "veritable" (true) capacity of the electrode which is corresponds to constant value of adsorption.

In the works,[1,2] authors investigated the kinetic mechanism of adsorption of the organic substances on the metallic electrode in two limited cases of electrode processes: diffusion and adsorption. In the present work we make an attempt to analyze the behaviour of Frumkin and Melik Gaykazan model in the galvanodynamic and potentiodynamic rejimes of functioning of the electrochemical system.

2 Theoretical analysis

2.1 Galvanodynamic rejime

The operational impedance of the equivalent electric which is represented in Figure 1 may be exemplified in the form of relationship

$$Z(p) = R_{11} + \frac{W_{11}}{\sqrt{p}} + \frac{1}{p(C_A + C_{11})} \qquad (1)$$

where Z_{W11} is diffusion constant of the Warburg; p is the complex variable. In the galvanodynamic rejime (in the method of linear current scan) I(t)=I_0+ϑ t (where I_0 is the initial current value, is the rate of linear current scan), then at I_0 = 0, the Laplace operator of function I(t) is $I(p) = \vartheta/p^2$.[5]

So far as $E(p) = I(p) \cdot Z(p)$, the following expression is obtained for the operator potential

$$E(p) = \frac{\vartheta}{p^2}\left[R_{11} + \frac{W_{11}}{\sqrt{p}} + \frac{1}{p(C_D + C_{11})}\right] \qquad (2)$$

Using invers Laplace transform tables[6] we obtained the following expression for the potential

$$E(t) = \vartheta R_{11} t + \frac{\vartheta W_{11} \cdot 4 \cdot t^{3/2}}{1 \cdot 3 \cdot 5 \cdot 3\sqrt{\pi}} + \frac{\vartheta t^2}{(C_D + C_{11})\, 2!} \qquad (3)$$

Potential *vs.* time dependence plotted according to equation (3) is shown in the Figure 2, which is plotted for the following parameters of equivalent circuit: $R_{11} = 5\,Ohm \cdot cm^2$;$W_{11} = 50\,Ohm \cdot cm^2 \cdot S^{(-1/2)}$; $C_D = C_{11} = 100 \cdot 10^{(-6)} F/cm^2$; $\vartheta = 5 \cdot 10^{(-6)} A/S$.

The basic deposit (contribution) to E t-dependence in the equation (3) introduced the third member.

As it is shown from the Figure 2 and as it is followed from the equation (3) potential-time dependence has the second order parabolic character. In that way the parabolic character of potential-time dependence may be

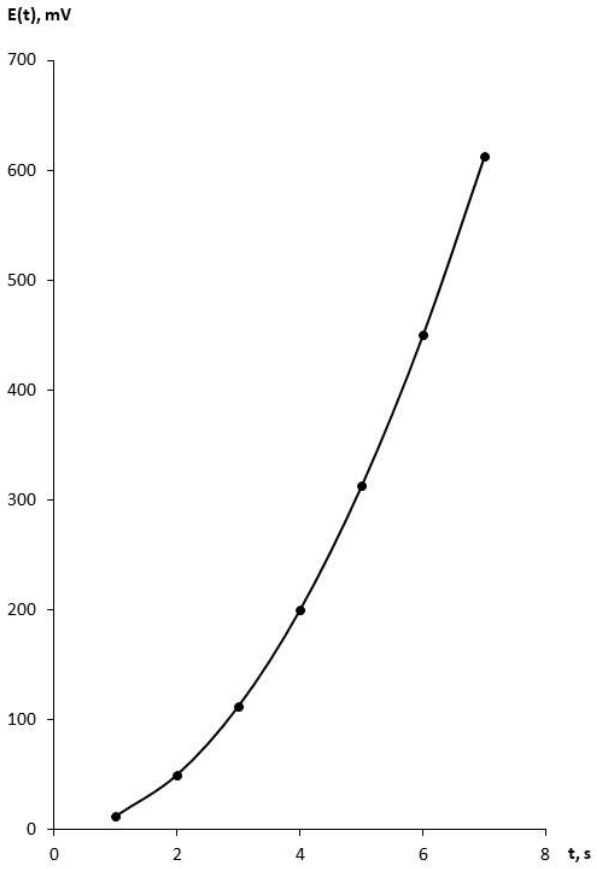

Figure 2. Potential *vs.* time dependence plotted according to equation (3) in the galvanodynamic rejime of functioning of the cell in the Frumkin and Melik-Gaykazan model

serve the evident proof of implementation of the equivalent electric scheme of Frumkin and Melik-Gaykazan model.

2.2 Potentiodynamic rejime

In the potentiodynamic rejime (in the method of linear potential scanning)$E(t) = E_0 + \vartheta t$ (where E_0 is the initial potential value and ϑ is its linear scan rate), then at E_0 = 0, the Laplace operator of function E(t) is $E(p) = \vartheta/p^2$. However, because $I(p) = E(p)/Z(p)$, then by substituting the values *E(p)* and *Z(p)* into the later expression, we obtained

$$I(p) = \frac{\vartheta a'}{p\left(p + \sqrt{p}c' + m\right)} \qquad (4)$$

The following designations are substituted into equation (4): $a = C_D + C_{11}$; $b = R_{11}(C_D + C_{11})$; $c = W_{11}(C_D + C_{11})$; $a' = a/b$; $c' = c/b$; $m = 1/b$.

Equation (4) can be expanded into the sum of partial

fractions

$$I(p) = \frac{\vartheta a'}{p\left(p + \sqrt{p}c' + m\right)} = \frac{d_1}{p} + \frac{d_2}{\sqrt{p} + m_2} + \frac{d_3}{\sqrt{p} + m_1} \tag{5}$$

Where m_1 and m_2 are the roots (zero) of the characteristic square equation $p + \sqrt{p}c' + m = 0$, which are equal to m_1=-72,36; m_2=-27,64.

The values of roots of square equation are determined at the following magnitude of the parameters of the equivalent electric circuits:
$W_{11} = 500$ Ohm $\cdot$ cm$^2 \cdot$ s$^{-1/2}$; $R_{11} = 5$ Ohm $\cdot$ cm^2; $C_A = C_{11} = 50 \cdot 10^{-6} F/\text{cm}^2$.

For the calculation of the while unknown coefficients we bring the equation (5) to the following appearance

$$I(p) = \frac{\vartheta a'}{p\left(p + \sqrt{p}c' + m\right)} = \frac{d_1\left(\sqrt{p} + m_1\right)\left(\sqrt{p} + m_2\right) + d_2 p\left(\sqrt{p} + m_1\right) + d_3 p\left(\sqrt{p} + m_2\right)}{p\left(\sqrt{p} + m_1\right)\left(\sqrt{p} + m_2\right)} \tag{6}$$

Coefficients d_1, d_2 and d_3 can be found by equating the factor at similar p powers in the numerators on the left and on the right.[7]

$$\left.\begin{array}{c} d_1 m_1 m_2 = \vartheta a' \\ d_1 + d_2 m_2 + d_3 m_1 = 0 \\ d_1 m_1 + d_2 m_2 = 0 \\ d_2 + d_3 = 0 \end{array}\right\} \tag{7}$$

The thus found coefficients d_1, d_2 and d_3 are $d_1 = \frac{\vartheta a'}{m_1 m_2}$; $d_2 = -\frac{d_1}{m_2 - m_1}$; $d_3 = -d_2$.

Using inverse Laplace transform tables[6] it is possible to carry out the term-by-term transformation of equation (5) into the space of original function. As a result, we obtained the following expression for the current

$$I(t) = d_1 + d_2\left[\frac{1}{\sqrt{\pi t}} - m_1 \exp(m_1^2 t)\text{erfc}\left(m_1 t^{1/2}\right)\right] + d_3\left[\frac{1}{\sqrt{\pi t}} - m_2 \exp(m_2^2 t)\text{erfc}\left(m_2 t^{1/2}\right)\right] \tag{8}$$

By taking into account the equality d_2+d_3=0, we obtained the following expression for the current

$$I(t) = d_1 + d_2 m_1 \exp(m_1^2 t)\text{erfc}\left(m_1 t^{1/2}\right) - d_3 m_2 \exp(m_2^2 t)\text{erfc}\left(m_2 t^{1/2}\right) \tag{9}$$

The numerical values of the coefficients d_1, d_2 and d_3 are equal to:
$d_1 = 100\ \mu A/\text{cm}^2$; $d_2 = 2,2361$; $d_3 = -2,2361$.

The final calculation of the current through the electrolytic cell can be conduct on the equation (10)

$$I(t) = 100\ \mu A/\text{cm}^2 + 2,2361 \cdot 72,36 \exp(5235,96 \cdot t)\ \text{erfc}\ (-72,36\times) - 2,2361 \cdot 27,64 \exp(763,96 \cdot t)\ \text{erfc}\left(-27,64 \cdot t^{1/2}\right) \tag{10}$$

Current-time dependence plotted based on equation (10) is represented in Figure 3, which is plotted for the indicated above equivalent circuit parameters and linear scan rate of potential $\vartheta = 1V/s$.

It is shown from Figure 3 that the current-time dependence in the case fulfilment of Frumkin and Melik-Gaykazan model has the rectilinearity character.

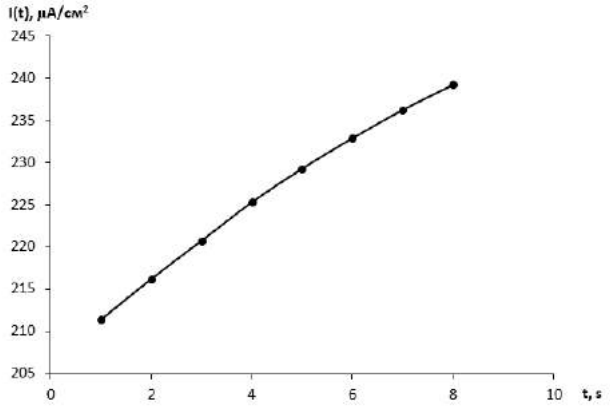

Figure 3. Dependance current *vs.* time plotted based on equation (10) in the potentiodynamic rejime de of functioning of the Frumkin and Melik-Gaykazan model

3 Conclusion

By the graphic analytical method are disclosed the two essential indications which are confirmed a presence in the electrochemical system the Frumkin and Melik-Gaykazan model (or scheme).

On the one hand this is the submission of the potential time dependence to parabola of second order in the galvanodynamic rejime ode of functioning of the electrochemical cell. On the other hand, the submission the current time dependence to linear function in the potentiodynamic rejime.

References

[1] Frumkin FN. The determination of a adsorption kinetic of the organic substances by method of measuring of capacitance and conduction of electrode-solution interface by alternating current method, in Electrode Processes, Nauka, Russia, 1987, 291-295.

[2] Frumkin AN. MelikGaykazan VI, Doklady of Academy of Sciences of USSR, Russia, 1951, **77**(5): 855-858.
[3] Damaskin BB, Petry OA. MelikGaykazan VI, Introduction to the Electrochemical Kinetics, Vyschaya Scholar, Russia,175: 143.
[4] Grafov BM, Ukshe EA.The Electrochemical circuites of alternating current, Nauka, Russia, 1973, 28-32.
[5] Kontorovich MI. The Operational calculus and Processes in Electrical Circuites, Soviet Radio, Russia, 1975, 320.
[6] Abramovich EM, Stigan I. Hanbook on Spesial Functions, Nauka, Russia, 1973, 80.
[7] Dech G, Rukovodstvo K. Practicheskomu primeneniy preobrazovaniia Laplasa, Moscow, Russia,Nauka Publ, 1965, 287.

Mater Eng Res, 2019, 1(1): 11-14
DOI: 10.25082/MER.2019.01.002

RESEARCH ARTICLE

Behaviour of the electrochemical intrgrator on the basis of solid electrolyte in galvanoharmonic charging mode

R. M. Guseynov* R. A. Radzhabov E. A. Medzhidova

Abstract: Behaviour of the Electrochemical integrator on the basis of Solid Electrolyte is studied in the galvanoharmonic charging mode. The possibility of application of simpler and more graphic calculation technigue and separation of impedance of electrochemical systems into active and reactive components is shown. The plotting of the dependences of the active and reactive impedance components on ac freguency was used to find the values of parameters of the studied equivalent electric cuircuits.

Keywords: electrochemical integrator, solid electrolyte, operational impedance, galvanoharmonic charging mode

1 Introduction

The investigation of the electrochemical behavior of the integrator was performed by operation impedance method which is based on the Laplas transformation and Ohms low between current, voltage and complex resistance (impedance). And what is more in this article was performed the new method of separating of the impedance into active and reactive components.

The basic constructive element of the electrochemical integrator on the basis of solid electrolyte is the electrolytic cell which contains the reversible silver electrode and the inert coal or graphite electrode. The solid electrolyte Ag_4RbI_5 is placed between two electrodes.

The electrochemical integrator may be represented schematically in the next form

$$(\,-\,)\; Ag|Ag_4RbI_5|C\;\;(+) \qquad (1)$$

Equivalent electric circuit of a cell with the blocked electrode- solid electrolyte interface C / Ag_4RbI_5 can be presented in the form of (Figure 1) where R_e is the resistance of solid electrolyte; C_2 is the adsorbtion desorbtion capacitance; Z_{W2} diffusion impedance of Warburg related to the sublattice defects of the solid electrolyte.

Figure 1. Equivalent electric circuit of the electrochemical integrator (ionix) on the basis of solid electrolyte Ag_4RbI_5

In this work we study the behavior of the electrochemical integrator (ionix) in the mode of galvanoharmonic charging of the electrode solid electrolyte interface.

2 Thoretical analysis

In the course of ionix charging on the silver electrode cathode the electrodeposition takes place according to equation $Ag^+ + e = Ag$.

On the graphite electrode the charging of double electric layer process takes place. Owing to a small electronic conductivity of the solid electrolyte Ag_4RbI_5 (τ_e)= 10^-11ohm$^-1\cdot$ cm$^-1$[1] the double layer capacity C_2 is retained without change.

Operational impedance of a cell shown in Figure 1 can be presented in the form of

$$Z(p) = R_e + \frac{W_2}{\sqrt{p}} + \frac{1}{pC_2} \qquad (2)$$

where W_2 is diffusion impedance of Warburg connected with the diffusion of the sublattice defects of the solid electrolyte; C_2 is the capacitance of double electric layer; R_e is active or Ohmic resistance.

So far as the current is applyd in the galvanoharmonic mode $I(p) = I_o\frac{\omega}{p^{2+\omega^2}}$ the operational voltage can be presented in galvanoharmonic mode also, as

Received: January 7, 2019 **Accepted:** January 23, 2019 **Published:** January 28, 2019

*Correspondence to: R.M. Guseynov, Dagestan State Pedagogical University, Makhachkala, Russia; Email: rizvanguseynov@mail.ru

Citation: Guseynov RM, Radzhabov RA and Medzhidova EA. Behaviour of the electrochemical intrgrator on the basis of solid electrolyte in galvanoharmonic charging mode. *Mater Eng Res*, 2019, **1**(1): 11-14.

$$E(p) = I_o \frac{\omega}{p^{2+\omega^2}} \left[R_\varepsilon + \frac{W_2}{\sqrt{p}} + \frac{1}{pC_2} \right] \tag{3}$$

where I_0 is the amplitude of the wave current; is the angular frequency. To obtain the primitive function of *E(t)* one has to carry out term- by- term transformation of expression (3) into the original function space. Let us designate the transformation operation as $\ll\overset{\cdots}{\longrightarrow}\gg$. Herewith, it is obvious that[2–4]

$$R_e I_o \frac{\omega}{p^2+\omega^2} \overset{\cdots}{\longrightarrow} I_o R_e \sin \omega t \tag{4}$$

The other terms in expression (3) can be transformed using the convolution technique,[5] whereby one can write the following relationships;[6]

$$I_o \frac{\omega}{p^2+\omega^2} \cdot \frac{1}{C_{2P}} \overset{\cdots}{\longrightarrow} \int_o^{t-\infty} \frac{I_o}{C_2} \sin \tau d\tau = -\frac{I_o}{\omega C_2} \cos \omega t \tag{5}$$

$$I_o \frac{\omega}{p^2+\omega^2} \cdot \frac{W_2}{\sqrt{p}} \overset{\cdots}{\longrightarrow} \int_o^{t\to\infty} I_o W_2 (t-\tau)^{-\frac{1}{2}} \sin \tau d\tau = \frac{I_o W_2}{\sqrt{\omega}} \Gamma(\frac{1}{2}) \sin \frac{1}{2}\pi \frac{1}{2} = \frac{I_o W_2}{\sqrt{\omega}} \Gamma(\frac{1}{2}) \sin \frac{\pi}{4} \tag{6}$$

where $\Gamma(\frac{1}{2}) = \sqrt{\pi}$- is the gamma function.

With account for relationship (4) (6), expression (3) for voltage assumes the form of

$$E(t) = I_o R_e \sin \omega t - \frac{I_o}{C_2 \omega} \cos \omega t + \frac{I_o W_2}{\sqrt{\omega}} \Gamma(\frac{1}{2}) \sin \frac{\pi}{4} = E_O \sin(\omega t - \theta) \tag{7}$$

where E_o is the ac voltage amplitude; θ is the current voltage phase angle.

Equation (7) follows from the theory of linear ac circuit,[4] according to which imposing sine wave current on the cell results in the sine wave voltage response in the circuit with similar angular frequency θ in the steady state mode.

Equation (7) must be correct at any time *t*. In particular, $\omega t = 0$ and $\omega t = \frac{\pi}{2}$, the two following relationships can be obtained on the basis of expression (7)

$$-\frac{I_o}{\omega C_2} + \frac{I_o W_2}{\sqrt{\omega}} \sqrt{\pi} \frac{\sqrt{2}}{2} = -E_o \sin \theta \tag{8}$$

$$I_o R_e + \frac{I_o W_2}{\sqrt{\omega}} \sqrt{\pi} \frac{\sqrt{2}}{2} = E_o \cos \theta \tag{9}$$

$$\begin{cases} \frac{I_O}{\omega C_2} - \frac{I_O W_2}{\sqrt{\omega}} \sqrt{\pi} \frac{\sqrt{2}}{2} = E_o \sin \theta \\ I_O R_e + \frac{I_o W_2}{\sqrt{\omega}} \sqrt{\pi} \frac{\sqrt{2}}{2} = E_o \cos \theta \end{cases} \tag{8a, 9a}$$

As seen in the vector diagram (Figure 2), any sine wave voltage can be formally sepated into an active and reactive components[6] corresponding to:

$$E_o \sin \theta = E_{react}$$

$$E_o \cos \theta = E_{act}$$

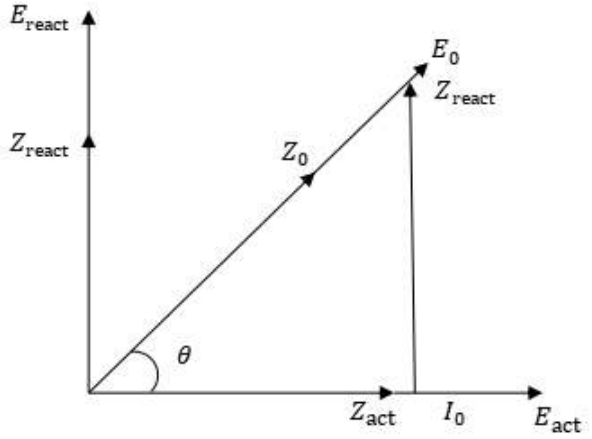

Figure 2. Vector diagram showing the relationship between the voltage triangle and resistance triangle

Division of relationship (8) and (9) by current I_o allows passing from the voltage triangle to the resistance triangle in which reactive E_{react} and active E_{act} impedance components are:

$$Z_{react} = \frac{1}{\omega C_2} - \frac{W_2}{\sqrt{\omega}} \sqrt{\pi} \frac{\sqrt{2}}{2} \tag{10}$$

$$Z_{act} = R_e + \frac{W_2}{\sqrt{\omega}} \sqrt{\pi} \frac{\sqrt{2}}{2} \tag{11}$$

Division of relationship (10) by relationship (11) yields the expression for the slope of the electrode impedance phase angle:

$$tg\theta = \frac{Z_{react}}{Z_{act}} \tag{12}$$

Figure 4 shows the impedance complex plane plot of the electrochemical integrator calculated according to

expression (10) and (11) at the following values of the equivalent electric circuit parameters: $R_e = 4\ Ohm \cdot cm^2$; $C_2 = 13,3 \cdot 10^{-6}\ F/cm^2$; $W_2 = 50\ Ohm \cdot cm^2 \cdot s^{-1/2}$

The phase angle of electrode impedance tends to at a decrease in the ac frequency and tends to 90^0 at increase in the ac frequency and tends to 0^0 at increase in the ac frequency (Figure 3).

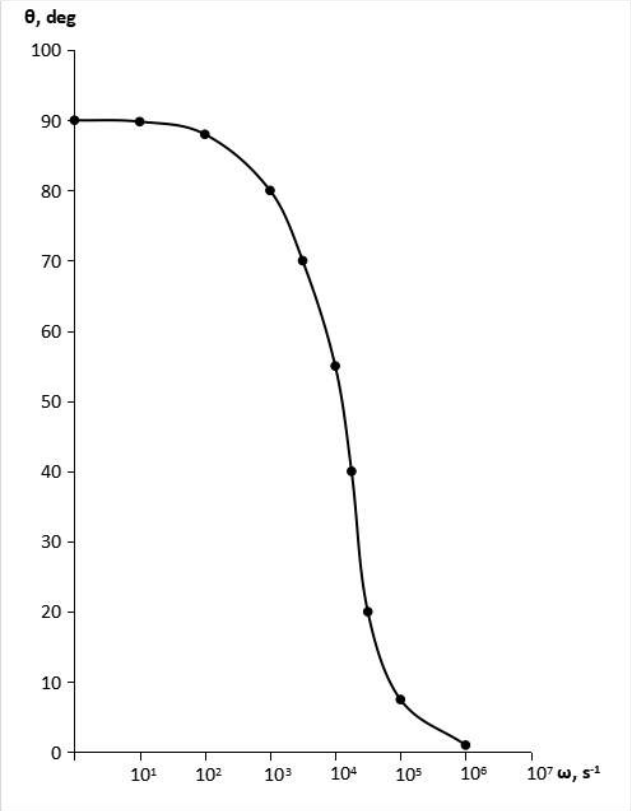

Figure 3. Frequency dependence of the impedance phase angle of a electrochemical integrator

As seen in Figure 4 the slope of the impedance complex plane plot to the active resistance axis is decreased at increasing of ac frequency.

The absolute impedance of the electrochemical integrator calculated according to relationship (13)

$$|Z| = \sqrt{Z_{act}^2 + Z_{react}^2} \qquad (13)$$

can be presented in the form of the following expression

$$Z = \left\{ R_e^2 + \frac{W_2^2 \pi}{\omega} + \frac{W_2\sqrt{\pi}}{\sqrt{\omega}2}(2R_e - \frac{2}{c_2\omega}) + \frac{1}{c_2^2\omega^2} \right\}^{\frac{1}{2}} \qquad (14)$$

The dependence of the absolute impedance on the ac frequency is shown in Figure 5. According to relationship (14), the absolute impedance tends at an increase in a frequency to a constant value equal to resistance R_e of the solid electrolyte.

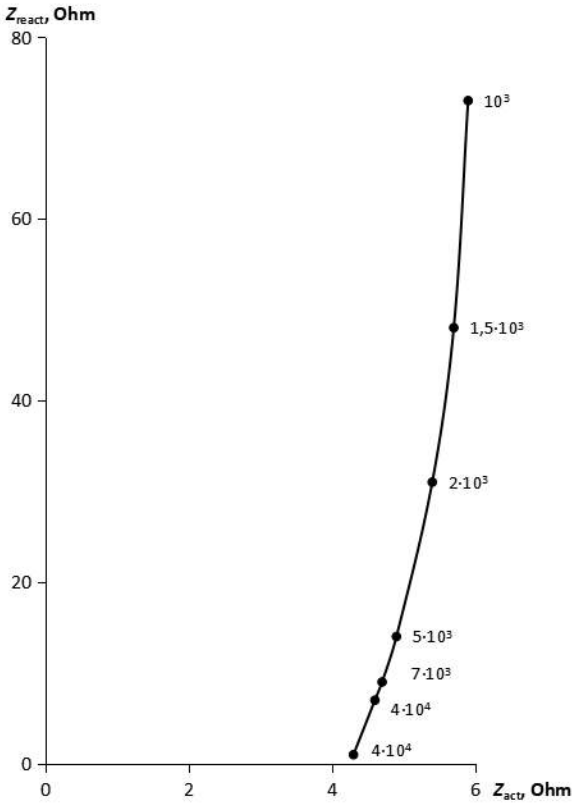

Figure 4. Impedance complex plane plot of electrochemical integrator. Numbers near the points correspond to the angular frequency values in Hz.

For plotting the experimental results it is convenient to reduce expression (10) to the form of

$$Z_{react}\omega = \frac{1}{c_2} - \frac{w_2\sqrt{2\pi}}{2}\sqrt{\pi} \qquad (10a)$$

The plot corresponding to relationship (10a) is shown in Figure 6, it can be used to estimate the value of parameters C_2 and W_2.

The dependence of active impedance component Z_{act} on the frequency according to equation (11) is shown in Figure 7.

The plot of function $Z_{act} - f\left(\frac{1}{\sqrt{\omega}}\right)$ $at\ \omega \to \infty$ approaches the constant value equal to R_e.

3 Results and conclusion

In this article we were obtained frequency dependances of impedance, frequency dependence of the impedance phase angle, of the absolute impedance and the frequency dependances of the active and reactive

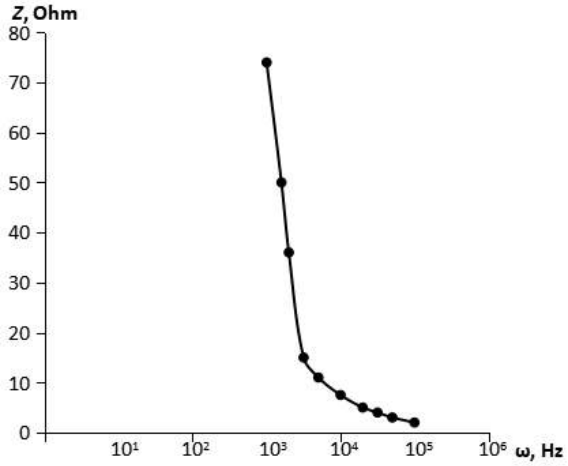

Figure 5. Dependance of absolute impedance of electrochemical integrator on ac frequency

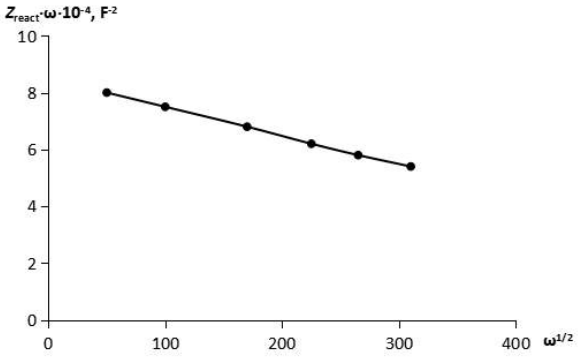

Figure 6. Determination of C_2 and W_2 according to equation (10a)

components of the impedance of the electrochemical integrator on the basis of the solid electrolyte. This work uses a new method based on the results of the throry of linear ac circuits for calculation and factori zation of impedance into active and reactive components. Conclusion. One should note that the method of calculation and separation of impedance into components used in this work is simple and graphic, which in our opinion, makes the operational methods especially attractive for analysis of properties of ac circuits.

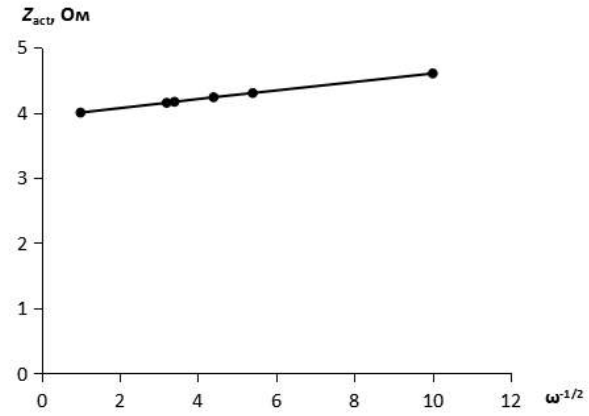

Figure 7. Determination R_ε in according to equation (11)

References

[1] Ukshe EA and Bukun NG. Solid Electrolytes. *Moscow: Nauka*, 1977, 176.

[2] Guseynov RM, Makhmudov HM, Radzhabov RA, *et al*. Behaviour of blocked (inert) electrode / Solid Electrolyte Interface or ionic melt in Galvanoharmonic Charging Mode. Case of decelerated diffusion and adsorption desorption of two different kinds of particles. *Melts*, 2016, **1**: 14-25.

[3] Guseynov RM and Radzhabov RA. Behaviour of Blocked Electrode Solid Electrolyte Interface in Galvanoharmonic Charging Mode. *Russian Journal of Electrochemistry*, 2015, **51**(4): 325-331. https://doi.org/10.1134/S1023193515040060

[4] Ryzhik IM. Tablitsy integralov, sum, rydov I proizvedeniy. M-L, 1948, 151.

[5] Guseynov RM. Relaxation Processes in Solid Electrilytes. *Moscow: Nauka Publ*. 1993, 160.

[6] Neiman LR and Demirchan KS. Theoretical bases of electrical engineer, *Leningrad Energy Publ*, 1967, 552.

Mater Eng Res, 2019, 1(1): 15-19
DOI: 10.25082/MER.2019.01.004

RESEARCH ARTICLE

One-step synthesis of TiO_2 nanoparticles using simple chemical technique

Majid Farahmandjou

Abstract: Titanium dioxide nanoparticles (TiO_2) have been extensively investigated because of its high chemical sustainability, optic properties, and adaptation to the environment. These studies include applications in heterogeneous catalysts, solar cells, coating technology, and electrical devices. TiO_2 particles in the nanometer scale can remove limitations, such as the absorbance of organic materials, because of a high surface area to volume ratio. Titanium dioxide nanoparticles, were synthesized using a simple wet chemical method. Their physico-chemical properties were characterized by transmission electron microscopy (TEM), scanning electron microscopy (SEM) and X-ray diffraction (XRD) analyses. The TEM results showed that the mean size of as-synthesized TiO_2 was 5 nm with high crystalline anatase phase. The SEM observations revealed that the size of nanoparticles increased with annealing temperature and the morphology of the particles changed to the spherical shape. The crystal structure of the nanoparticles before and after annealing was done by XRD analysis. The rutile phase was formed after heat treatment at 600^{o}C for 3 hours.

Keywords: TiO_2 nanoparticles, wet chemical synthesis, rutile phase

1 Introduction

Metal oxides have recently become widely used in the field of medical and industrial applications[1–25] . TiO_2 nanoparticles have attracted attention in the fields of environmental purification, solar energy cells, photocatalysts, gas sensors, photo electrodes and electronic devices. It has been widely used as a pigment in paints, ointments, toothpaste etc[26] . Nanosized TiO_2 particles are of particular interest due to their specifically size-related properties. Generally it is in three forms, anatase (tetragonal, a=b=3.78 $\mathring{A}$, c=9.5 $\mathring{A}$), rutile (tetragonal, a=b=4.58 $\mathring{A}$, c=2.95 $\mathring{A}$) and brookite (rhombohedral, a=5.43 $\mathring{A}$, b=9.16 $\mathring{A}$, c=5.13 $\mathring{A}$). Among various phases of titania reported, anatase shows a better photocatalytic activity and antibacterial performance[27] . A stable anatase up to the sintering temperature of the ceramic substrates is most desirable for applications on antibacterial self-cleaning building materials like bathroom tile, sanitary ware and self-cleaning applications[28] . Anatase-to-rutile transformation is usually occurs at 600 to 700°C[29] . Phase transition to rutile is nonreversible because of the greater thermodynamic stability of rutile phase[30] . There are several factors in determining the important properties such as the particle size, crystallinity and morphology that affect in the performance of TiO_2 in applications[31] . A number of studies have focused on the synthesis of titanium dioxide nanoparticles[32] . Anatase and rutile are commonly obtained by hydrolysis of titanium compounds, such as titanium tetrachloride ($TiCl_4$)[33] or titanium alkoxides ($Ti(OR)_4$), in solution[34] . Brookite is sometimes observed as a by-product of the precipitation reaction carried out in acidic medium at low temperature.[34,35] Brookite is also obtained as large crystals by hydrothermal methods at high temperature and pressure in aqueous[36] or in organic media[37] . In the present work, we focused on synthesis of TiO_2 nanoparticles system by wet chemical route. This method has novel features which are of considerable interest due to its low cost, easy preparation and industrial viability. Synthesis of rutile form by wet synthesis technique is reported by $TiCl_4$ solution precursor and calcined at 600^{0}C. The structural and optical properties of TiO_2 have been studied by XRD, SEM and TEM analyses.

2 Experimental detail

TiO_2 nanoparticles were synthesized by a new approach according to the following manner. 20 mL NaOH

Received: March 28, 2019 **Accepted:** April 11, 2019; **Published:** April 13, 2019

*Correspondence to: Majid Farahmandjou, Department of Physics, Varamin Pishva Branch, Islamis Azad University, Varamin, Iran; Email: farahmandjou@iauvaramin.ac.ir

Citation: Farahmandjou M. One-step synthesis of TiO2 nanoparticles using simple chemical technique. *Mater Eng Res*, 2019, **1**(1): 15-19.

solution (64.8 g/l) was added drop wise into 100 mL deionized water with stirring. Then, 5cc $TiCl_4$ solution (200 g/l) was added drop wise to the solution and stirred for 5 min at room temperature. At first a large amount of HCl gas was exhausted during the mixing process and then light yellow solution was obtained. Resulting TiO_2 slurry and an aqueous solution of HNO_3 (2 mL) were dried at 65^0C for 1 h, cooled to room temperature and neutralized with 26% of aqueous ammonia (10 mL) and stirred again for 10 min. The pH was adjusted by adding nitric acid in the range for 2.0 to 2.5. Then, the product was aged at 220^oC for 2.5 hours and finally calcined at 600^0C for 3 hours. The white TiO_2 powder was later obtained.

The specification of the size, structure and optical properties of the as-synthesis and annealed TiO_2 nanoparticles were carried out. X-ray diffractometer (XRD) was used to identify the crystalline phase and to estimate the crystalline size. The XRD pattern were recorded with 2θ in the range of 4-85^o with type X-Pert Pro MPD, Cu-K_α: λ = 1.54 $\mathring{A}$. The morphology was characterized by field emission scanning electron microscopy (SEM) with type KYKY-EM3200, 25 kV and transmission electron microscopy (TEM) with type Zeiss EM-900, 80 kV.

3 Results and discussion

X-rar diffraction (XRD) at 40Kv was used to identify crystalline phases and to estimate the crystalline sizes. Figure 1(a) shows the XRD morphology of TiO_2 nanoparticles and indicates the structure of tetragonal anatase phase. The XRD patterns showed this sample have four sharp peaks 2θ angle at the peak position at 25.2^o, 37.7^o, 47.8^o, 54.1^o, 62.5^o, 69.4^o and 75.5^o with (101), (004), (200) , (105), (211), (204) and (116) diffraction planes, respectively are in accordance with the TiO_2 anatase phase. It can be seen the peak position at 27.5^o corresponds to the plane (110) of rutile form. The mean size of the ordered TiO_2 nanoparticles has been estimated from full width at half maximum (FWHM) and Debye-Sherrer equation.[38]

Where, 0.89 is the shape factor, λ is the x-ray wavelength, B is the line broadening at half the maximum intensity (FWHM) in radians, and θ is the Bragg angle. The mean size of as-prepared TiO_2 nanoparticles was 5.5 nm from this Debye-Sherrer equation.

Scanning electron microscope (SEM) was used for the morphological study of nanoparticles of TiO_2. These figures show that high homogeneity emerged in the samples surface by increasing annealing temperature. With increasing temperature the morphology of the particles

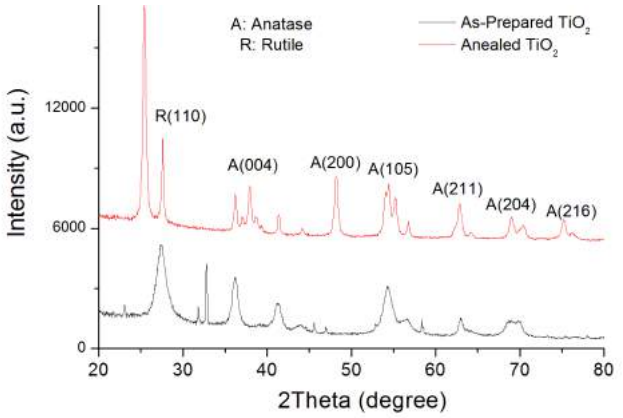

Figure 1. XRD pattern of as-prepared and annealed TiO_2 nanoparticles

changes to the spherical shape and nanopowders were less agglomerate. Figure 2(a) shows the SEM image of the as-prepared TiO_2 nanoparticles with spherical shape prepared by wet chemical method. Figure 2(b) shows the SEM image of the annealed TiO_2 nanoparticles. The TiO_2 nanoparticles formed were not agglomerated. The spherical shaped particles with clumped distributions are visible through the SEM analysis. The average crystallite size of annealed nanocrystals is about 25 nm. Figure 3 indicates the commercial TiO_2 nanoparticles.

The transmission electron microscopic (TEM) analysis was carried out to confirm the actual size of the particles, their growth pattern and the distribution of the crystallites. Figure 3 shows the as-synthesized TEM image of titanium dioxide prepared by wet synthesis. It is observed that the anatase TiO_2 nanoparticles are built with a diameter of 5nm. The principal novelty of the procedure developed is that it results in nanoparticles of TiO_2, with a regular distribution, uniform size and spherical shape because of HNO_3 stabilizer.[39,40]

4 Conclusion

Titanium dioxide nanoparticles were successfully prepared by simple and new wet synthesis method. Anatase TiO_2 is obtained from wet synthesis method and rutile phase is obtained when it is calcined at 600 ^{o}C. The average size of annealed TiO_2 is about 25 nm. TEM studies show spherical structure of TiO_2 nanoparticles with size of 5nm for smallest particle. SEM images showed that with increasing temperature the morphology of the particles changes to the spherical shape and nanopowders were less agglomerate. XRD pattern of TiO_2 nanoparticles indicated the structure of tetragonal anatase phase without annealing and rutile phase with annealing process at 600 ^{o}C.

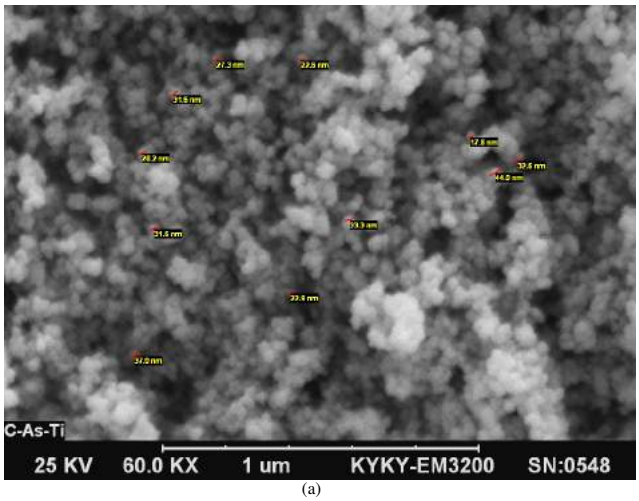

(a)

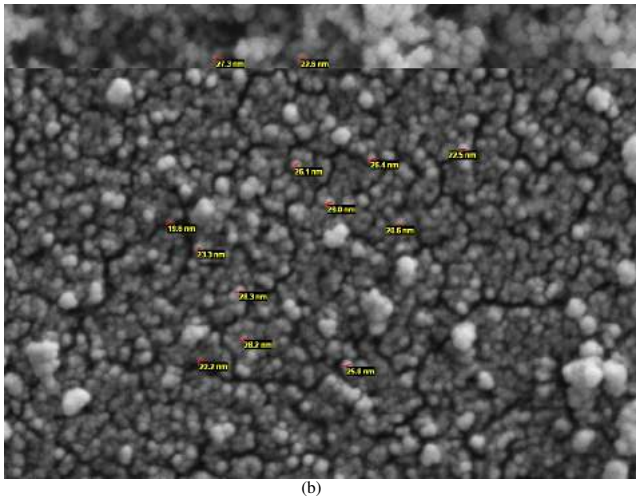

(b)

Figure 2. SEM images of the (a) as-prepared (b) annealed at 600^0C

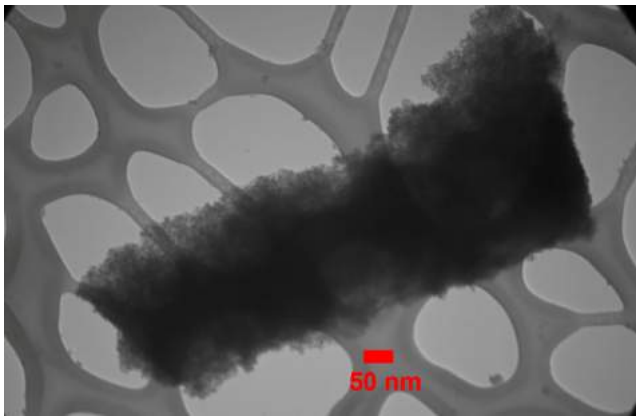

Figure 3. TEM image of the as-prepared TiO_2 nanoparticles

5 Acknowledgments

The authors are thankful for the financial support of varamin pishva branch at Islamic Azad University for analysis and the discussions on the results.

References

[1] Jurablu S, Farahmandjou M and Firoozabadi TP. Multiple-layered structure of obelisk-shaped crystalline nano-ZnO prepared by sol-gel route. Journal of Theoretical and Applied Physics, 2015, **9**: 261-266. https://doi.org/10.1007/s40094-015-0184-6

[2] Farahmandjou M and Soflaee F. Polymer-Mediated Synthesis of Iron Oxide (Fe_2O_3) Nanorods. Chinese Journal of Physics, 2015, **53**: 080801-080809. https://doi.org/10.6122/CJP.20150413

[3] Farahmandjou M and Soflaee F. Synthesis and characterization of α-Fe_2O_3 nanoparticles by simple co-precipitation method. Physical Chemistry Research, 2015, **3**: 193-198. https://doi.org/10.22036/pcr.2015.9193

[4] Zarinkamar M, Farahmandjou M and Firoozabadi TP. Diethylene Glycol-Mediated Synthesis of Nano-Sized Ceria (CeO_2) Catalyst. Journal of Nanostructures, 2016, **6**: 114-118. https://doi.org/10.7508/jns.2016.02.002

[5] Farahmandjou M. Magnetocrystalline properties of Iron-Platinum (L10-FePt) nanoparticles through phase transition. Iranian Journal of Physics Research, 2016, **16**: 1-5. https://doi.org/10.18869/acadpub.ijpr.16.1.1

[6] Farahmandjou M and Khalili P. Morphology Study of anatase nano-TiO_2 for Self-cleaning Coating. International Journal of Fundamental Physical Sciences, 2013, **3**: 54-56. https://doi.org/10.14331/ijfps.2013.330055

[7] Farahmandjou M and Ramazani M. Fabrication and Characterization of Rutile TiO_2 Nanocrystals by Water Soluble Precursor. Physical Chemistry Research, 2015, **3**: 293-298. https://doi.org/10.22036/pcr.2015.10641

[8] Shadrokh S, Farahmandjou M and Firozabadi TP. Fabrication and Characterization of Nanoporous Co Oxide (Co_3O_4) Prepared by Simple Sol-gel Synthesis. Physical Chemistry Research, 2016, **4**: 153-160. https://doi.org/10.22036/pcr.2016.12909

[9] Farahmandjou M, Honarbakhsha S and Behrouziniab S. PVP-Assisted Synthesis of Cobalt Ferrite ($CoFe_2O_4$) Nanorods. Physical Chemistry Research, 2016, **4**: 655-662. https://doi.org/10.22036/pcr.2016.16702

[10] Farahmandjou M and Golabiyan N. Solution combustion preparation of nano-Al_2O_3: synthesis and characterization. Transp Phenom Nano and Micro Scales, 2015, **3**: 100-105.

[11] Farahmandjou M. Synthesis of ITO Nanoparticles Prepared by Degradation of Sulfide Method. Chinese Physics Letters, 2012, **29**: 077306-077309. https://doi.org/10.1088/0256-307X/29/7/077306

[12] Farahmandjou M and Golabiyan N. Synthesis and characterization of Alumina (Al_2O_3) nanoparticles prepared by simple sol-gel method. Int J Bio-Inorg Hybr Nanomater, 2016, **5**: 73-77.

[13] Farahmandjou M. Synthesis and Structural Study of L10-FePt nanoparticles. Turkish Journal of Engineering and Environmental Science, 2010, **34**: 265-270. https://doi.org/10.3906/muh-1010-20

[14] Akhtari F, Zorriasatein S, Farahmandjou M, *et al*. Structural, optical, thermoelectrical, and magnetic study of $Zn_{1-x}Co_xO$ ($0 \leq x \leq 0.10$) nanocrystals. International Journal of Applied Ceramic Technology, 2018, **15**: 723-733.
https://doi.org/10.1111/ijac.12848

[15] Akhtari F, Zorriasatein S, Farahmandjou M, *et al*. Synthesis and optical properties of Co^{2+}-doped ZnO Network prepared by new precursors. Materials Research Express, 2018, **5**: 065015-065024.
https://doi.org/10.1088/2053-1591/aac6f1

[16] Khoshnevisan B, Marami MB and Farahmandjou M. Fe^{3+}-Doped Anatase TiO_2 Study Prepared by New Sol-Gel Precursors. Chinese Physics Letters, 2018, **35**: 027501-027505.
https://doi.org/10.1088/0256-307X/35/2/027501

[17] Khoshnevisan B, Marami MB and Farahmandjou M. Solgel Synthesis of Fe-doped TiO_2 Nanocrystals. Journal of Electronic Materials, 2018, **47**: 3741-3749.
https://doi.org/10.1007/s11664-018-6234-5

[18] Jafari A, Khademi S and Farahmandjou M. Nano-crystalline Ce-doped TiO_2 Powders: Sol-gel Synthesis and Optoelectronic Properties. Materials Research Express, 2018, **5**: 095008-095017.
https://doi.org/10.1088/2053-1591/aad5b5

[19] Farahmandjou M, Honarbakhsh S and Behrouzinia S. FeCo Nanorods Preparation Using New Chemical Synthesis. Journal of Superconductivity and Novel Magnetism, 2018, Accepted.
https://doi.org/10.1007/s10948-018-4659-y

[20] Farahmandjou M and Khalili P. Study of Nano SiO_2/TiO_2 Superhydrophobic Self-Cleaning Surface Produced by Sol-Gel. Australian Journal of Basic & Applied Sciences, 2013, **7**: 462-465.

[21] Jurablu S, Farahmandjou M and Firoozabadi TP. Sol-gel synthesis of zinc oxide (ZnO) nanoparticles: study of structural and optical properties. Journal of Sciences, Islamic Republic of Iran , 2015, **26**: 281-285.

[22] Farahmandjou M and Dastpak M. Fe-Loaded CeO_2 Nanosized Prepared by Simple Co-Precipitation Route. Physical Chemistry Research, 2018, **6**: 713-720.
https://doi.org/10.22036/pcr.2018.132220.1486

[23] Farahamndjou M. The study of electro-optical properties of nanocomposite ITO thin films prepared by e-beam evaporation. Revista mexicana de fsica, 2013, **59**: 205-207.

[24] Dastpak M, Farahmandjou M and Firoozabadi TP. Synthesis and preparation of magnetic Fe-doped CeO_2 nanoparticles prepared by simple sol-gel method. Journal of Superconductivity & Novel Magnetism, 2016, **29**: 2925-2929.
https://doi.org/10.1007/s10948-016-3639-3

[25] Motaghi S and Farahmandjou M. Structural and optoelectronic properties of Ce-Al_2O_3nanoparticles prepared by sol-gel precursors. Material Research Express, 2019, **6**(4): 045008.
https://doi.org/10.1088/2053-1591/aaf927

[26] Yuan S, Chen W and Hu S. Fabrication of TiO_2 nanoparticles/surfactant polymer complex film on glassy carbon electrode and its application to sensing trace dopamine. Materials Science & Engineering C, Biomimetic and, Supramolecular Systems, 2005, **25**(4): 479-485.
https://doi.org/10.1016/j.msec.2004.12.004

[27] Sakatani Y, Grosso D, Nicole L, *et al*. Optimised photocatalytic activity of grid-like mesoporous TiO_2 films: effect of crystallinity, pore size distribution, and pore accessibility. Journal of Materials Chemistry, 2006, 16: 77-82.

[28] Mills A and Wang J. Simultaneous monitoring of the destruction of stearic acid and generation of carbon dioxide by self-cleaning semiconductor photocatalytic films. Journal of Photochemistry and Photobiology B Biology, 2006, **182**(2): 181-186.
https://doi.org/10.1016/j.jphotochem.2006.02.010

[29] Kumar SR , PillaiSC , Hareesh US , *et al*. Synthesis of thermally stable, high surface area anatasealumina mixed oxides. Materials Letters, 2000, **43**(5-6): 286-290.
https://doi.org/10.1016/s0167-577x(99)00275-x

[30] Reidy DJ, Holmes JD and Morris MA. The critical size mechanism for the anatase to rutile transformation in TiO_2 and doped-TiO_2. Journal of the European Ceramic Society, 2006, **26**(9): 1527-1534.
https://doi.org/10.1016/j.jeurceramsoc.2005.03.246

[31] Lee KM, SuryanarayananV and Ho KC. A study on the electron transport properties of TiO_2 electrodes in dye-sensitized solar cells. Solar Energy Materials and Solar Cells, 2007, **91**(15-16): 1416-1420.
https://doi.org/10.1016/j.solmat.2007.03.007

[32] Sagadevan S. Synthesis and electrical properties of TiO_2 nanoparticles using a wet chemical technique. American Journal of Nanoscience and Nanotechnology, 2013, **1**: 27-30.
https://doi.org/10.11648/j.nano.20130101.16

[33] Santacesaria E, Tonello M, Storti G, *et al*. Kinetics of titanium dioxide precipitation by thermal hydrolysis. Journal of Colloid & Interface Science, 1986, **111**(1): 44-53.
https://doi.org/10.1016/0021-9797(86)90005-6

[34] Chemseddine A and Moritz T. ChemInform Abstract: Nanostructuring Titania: Control over Nanocrystal Structure, Size, Shape, and Organization. Cheminform, 1999, **2**: 235-245.
https://doi.org/10.1002/chin.199914280

[35] Music S, Gotic M, Ivanda M, *et al*. Chemical and micro structural properties of TiO_2 synthesized by sol-gel procedure[J]. Materials Science & Engineering B (Solid-State Materials for, Advanced Technology), 1997, **47**(1): 33-40.
https://doi.org/10.1016/s0921-5107(96)02041-7

[36] Keesmann I. Zur hydrothermalen Synthese von Brookit. Zeitschrift Für Anorganische Und Allgemeine Chemie, 1966, 346: 30-43.
https://doi.org/10.1002/zaac.19663460105

[37] Kominami H, Kohno M and Kera Y. Synthesis of brookite-type titanium oxide nano-crystals in organic media. Journal of Materials Chemistry, 2000, **10**(5): 1151-1156.
https://doi.org/10.1039/a908528i

[38] Scherrer P. Bestimmung der inneren Struktur und der Gröe von Kolloidteilchen mittels Röntgenstrahlen. Kolloidchemie Ein Lehrbuch. Springer Berlin Heidelberg, 1912.

[39] Farahmandjou and Majid. Effect of Oleic Acid and Oleylamine Surfactants on the Size of FePt Nanoparticles. Journal of Superconductivity and Novel Magnetism, 2012, **25**(6): 2075-2079.
https://doi.org/10.1007/s10948-012-1586-1

[40] Zarinkamar M, Farahmandjou M, Firoozabadi TP, One-step synthesis of ceria (CeO_2) nano-spheres by a simple wet chemical method. Journal of Ceramic Processing Research, 2016, **17**(3): 166-169.

Mater Eng Res, 2019, 1(1): 20-31
DOI: 10.25082/MER.2019.01.005

RESEARCH ARTICLE

A study on the deformation and crushing of copper tubing: experiments, theory & FE modelling

R.P. Turner

Abstract: A series of 250 mm lengths of copper tubing, of 15 mm outer diameter and 0.7 mm wall thickness, were studied to determine their deformation if they were pinched or crushed between rigid objects applying a given force, to replicate potential accidental damage suffered by the copper pipes during service. A finite element modelling framework was developed to simulate the crushing of a copper pipe the same dimensions as that used for experiments, and the experimental data allowed for a validation of the pipe crushing at approximately room temperature, to consider copper pipe carrying cold water. The FE modelling activity was then extended to consider the deformation of copper pipe at 80°C, carrying heated water at this temperature. The modelling agreed reasonably well with experiment, and applied forces of 1.5 kN began to deform the cold pipe, with the pipe collapsing on itself at loads of 6 kN. The heated pipe began to deform at roughly 1.25 kN. Lastly, theoretical flow calculations were performed to determine the Reynolds value, the flow velocity and the pressure loss and head loss per unit length of the deformed pipes, according to classical pipe flow calculation methods.

Keywords: simulation, fluid mechanics, finite element, pressure drop

1 Introduction

Copper tubing is commercially available as standard in all sorts of pipe diameter sizes, ranging from a small, thin walled pipe of 15 mm diameter and wall thickness 0.7 mm, to 80 mm diameter and approximately 2.0 mm wall thickness, for commercial plumbing requirements[1] . Typical uses for copper tubing include the supply of cold and heated water from a mains water line to a local tap or boiler unit[2] , or as a refrigerant fluid transportation line in a heating, ventilation and air-conditioning (HVAC) system[3] . Copper is used to produce these fluid (often water) carrying pipes for a number of reasons. It is anti-microbial (employing the oligodynamic effect)[4] , which can kills bacteria before build-up[4] , it generally does not leach harmful metals in to the fluid it carries, as opposed to some other metals that can much more readily leach out in to the fluid[5] , it is non-permeable[6] , it does not suffer from corrosion readily in the typical working environment[7] , it is a ductile metal that can be shaped more readily than other metals, and its ductility offers greater fracture toughness than some other metals[8] . It is also an abundant natural resource[2] , and further is readily recyclable, thus reducing the raw material costs.

However, it is the material's malleability at moderate temperatures[6] to allow for ease of pipe manipulation which is the predominant reason that it is so widely used. Yet, copper's relative malleability at low temperatures may also be considered a weakness of the material, as it does mean that the pipe is susceptible to sustaining damage whilst in-service, through accidental impact or through undesired trapping mechanisms whilst in service.

The raw copper material can come from either virgin or recycled copper routes, however copper is one of the most recycled metals, and the copper scrap is often obtained from stripping down industrially used copper electrical wire to the bare wire component. Recycled copper generally shows very little degradation of mechanical property[9] , along with the usual impact of recycling including concomitant environmental and cost benefits, meaning recycled copper is increasingly in demand[10] .

Copper is a FCC lattice structure, it is a dense metal (8,900 kgm^{-3}) with a melting temperature of 1083°C. It generally is a relatively unreactive metal, with noticeable oxidation only occurring over a period of many years. This oxidation layer, called a patina, actually protects the copper below from further atmospheric degradation, whilst offering minimal reduction in the material prop-

Received: March 27, 2019 **Accepted:** April 17, 2019; **Published:** April 19, 2019

* **Correspondence to**: R.P. Turner, School of Metallurgy & Materials, University of Birmingham, Birmingham B15 2TT, UK; Email: R.P.Turner@bham.ac.uk

Citation: Turner RP. A study on the deformation and crushing of copper tubing: experiments, theory & FE modelling. *Mater Eng Res*, 2019, **1**(1): 20-31.

erty.

Copper tubing is manufactured on a considerable scale, given the widespread use of the finished product across a vast number of industrial applications. In order to manufacture the copper tubing, the raw material must be fed in to a furnace and melted. For common tubing applications, the raw copper comes from high quality grades of recycled scrap copper (sometimes referred to as bare bright copper)[11] . This grade ensures that the recycled material is largely free from contaminants and other material, and free from any visible oxidation. Sections scrap of material eligible to be classed as bare bright copper must be thicker than 16 gauge[11] (approximately 1.59 mm thick).

The raw material copper is melted in a large reverberatory furnace. The melt is raised to approximately 1260 to 1300°C, well in excess of the melt point of copper (1083°C). The molten copper is then fire-refined by the introduction of oxygen, which reacts to form oxides much more readily with any impurities still within the melt[12] . The oxides of the impurities are less dense than the copper, and so float to the surface as slag. Small traces of copper oxide are removed using additions of phosphorus to react with the oxygen, leaving near pure copper. This recycled copper can reach roughly 99.9% purity, virtually as pure as copper produced from virgin ore[12] .

The molten copper is subsequently poured in to horizontally aligned, water-cooled graphite moulds. Grips then pull the now solidified copper log linearly within the mould, allowing space for further molten copper to be poured in to the gap created at the back. The process continues as such until the maximum length of copper log is created. Once the cylindrical log is produced via continuous casting, the copper billet is placed in to an extrusion press. The billet is heated to the required forming temperature, and is pierced using a mandrel. A ram is located at the back end of the extrusion chamber, forcing the heated copper over the mandrel and through an extrusion hole on the opposite side of the chamber to the ram. The size and shape of the hole which the heated, highly malleable copper is forced through dictates the extruded material size and shape. The hollow copper tubing that emerges from the extruder can then be drawn out further, using grips to contact the tube, and pulling it through further dies to reduce its outer diameter and its wall thickness to the relevant size required[13] .

The process of drawing serves to work-harden the copper[14] , thus drawn tube has improved material mechanical properties such as the fracture toughness, compared to prior to drawing. Work-hardening is achieved through small amounts of plastic deformation within the materials causing a saturation of dislocations[15] within the crystal structure of the copper.

One of the main advantages of tubing production using this type of extruded and drawn methodology is the seamless nature of the finished product, with homogenous property and microstructure throughout its outer wall, and its wall thickness[13] . As opposed to seamless tube, welded tubing is formed from a flat sheet of material that is subsequently rolled and welded longitudinally. The presence of the weld within rolled, welded tubing can cause in-service issues, especially for pressurised pipe systems. However, despite the extra manufacturing costs associated with the extrusion method compared to rolled and welded, an extruded and drawn seamless tubing component offers improved mechanical properties. Thus, the seamless tubing is desirable within industrial applications, especially when considering the expense and containment issues associated with a burst pipe.

The mechanical properties of copper largely depend upon its route of production; however it does have good toughness at low temperatures, has room temperature strength of roughly 190-250 MPa[16] , which can be further enhanced by cold work-hardening. As the temperature increases, the strength remains roughly constant up to approximately 70°C, before beginning to decrease, with an increasing gradient, up to approximately 200°C. The yield strength decreases very gradually from room temperature up to 200°C.

Finite element simulations concerning the structural integrity of a pipe component are not new, indeed there are numerous instances within the literature of FE or numerical modelling to analyse the structural integrity, strength, and associated residual stress field left behind after pipe welding[17–21] , or through impact and loading[22,23] , however most of these studies tended to be considering steel pipework. Thus, there is a considerable gap in the efforts of FE and numerical analysts to simulate accidental deformation, and the knock-on effect of fluid flow within a damaged pipe, for the copper pipes so prominently used.

2 Material and methods

Copper pipe of external diameter 15 mm, wall thickness of 0. 7 mm, and thus internal diameter of 13.6 mm, was used for experimental measurements of pipe deformation due to certain applied loads. An ESH Testing Ltd 100 kN load frame press was used to apply the fixed load on to the central portion of pipe, which was clamped in-between two jaws measuring 25 mm in width. The set-up can be seen in the schematic given in Figure 1.

The press and jaw arrangement were utilised to apply specified loads to the pipe, in order to crush the pipe, as a physical simulation of a pipe becoming trapped in service and deforming accordingly. The applied loads were, in increasing order; 1.5 kN, 2 kN, 2.5 kN, 3 kN and 6 kN. There was no further clamping, lubrication or equipment used. The bar and jaws were at a constant 15-20°C, as was the surrounding atmosphere at the room temperature of the laboratory, in order to replicate the cold pipe under service.

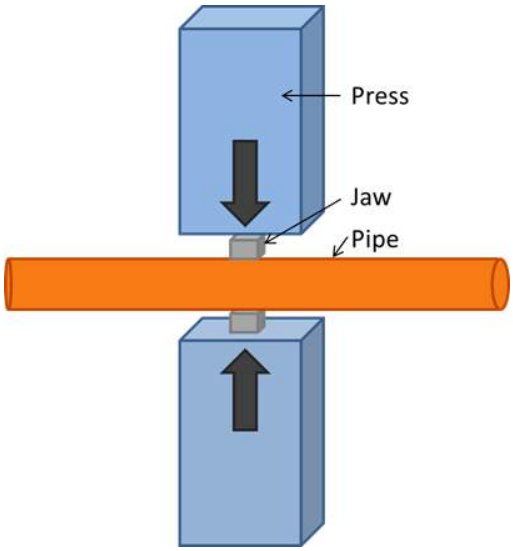

Figure 1. A schematic diagram showing the experimental set-up for deforming the pipe

3 Finite element modelling

An FE model was constructed using the Deform v11.2 software, from software developers SFTC[24] . The model was created using various rigid and plastically deformable objects. A plastically deformable workpiece was employed to represent the copper pipe. The model simulated a copper pipe of length 250 mm, with 15 mm outer pipe diameter and wall thickness of 0.7 mm. This was meshed by initially meshing the 2D cross-section of the pipe-wall with 2D quadrilateral elements, and then extruded through the length of the pipe to produce the 3D component. Hence, the elements were hexahedral, and numbered about 25,000 in the deformable workpiece.

The 3D pipe workpiece was assigned the properties of the copper material, with a Young's Modulus of 115GPa (at 15°C) or 105 GPa (at 80°C), a Poisson ratio of 0.33 and a temperature dependent flow stress given by the simplified Johnson-Cook Equation:

$$\bar{\sigma} = (A + B\bar{\epsilon}^n)\left[1 + C.ln\left(\frac{\dot{\epsilon}}{\dot{\epsilon_0}}\right)\right](1 - (T^*)^m) \quad (1a)$$

Where

$$T^* = \frac{T - T_{rm}}{T_{melt} - T_{rm}} \quad (1b)$$

And where $\bar{\epsilon}$ is the mean strain, $\dot{\epsilon}$the mean strain rate, T is operating temperature, $T_{rm}$is room temperature (15°C) and T_{melt} is melting temperature (1085°C),with further material dependent parameters *A, B, C, m, n,* $\dot{\epsilon_0}$ to be defined. In the case of copper, the values used are as given in Table 1.

These parameters to be fitted to match the material behaviour can largely be purely numerically quantified with little physical meaning, however analysing the form of the equation can inform that $\dot{\epsilon_0}$ is a reference strain rate, n is an exponent for the strain hardening, m is an exponent for the high temperature softening, and A is the base flow stress value when at room temperature, reference strain rate and zero strain.

Table 1. Parameters used to define the simplified Johnson-Cook flow stress equation

A	B	C	m	n	$\dot{\epsilon_0}$
123.7	435.1	0.022	0.83	0.31	1

Rigid (tooling) objects were used to apply a deformation within the FE model to match the experimental set-up accurately. Thus, cuboid blocks were created to represent the jaws of the compressing tooling that was used to provide the deforming force. As rigid objects experience no deformation, thus these did not require meshing. Boundary conditions between workpiece and rigid tooling, applied at nodes within the workpiece mesh that were in contact with a rigid object were assigned with a shear friction coefficient of 0.08, as is recommended for cold forging operations. The workpiece was also given a self-contact boundary condition for when the pipe inner walls fold and contact. A time step of 0.01 s was implemented, and automatic re-meshing of the workpiece was switched on. The set-up of the model can be seen in Figure 2.

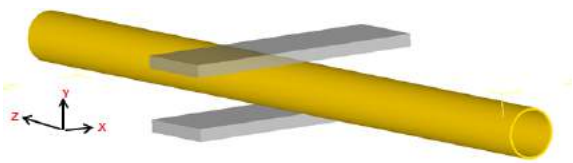

Figure 2. The FE modelling set-up, with the plastically deformable workpiece pipe, and rigid tooling

Two models, identical in set-up barring the pipe workpiece operating temperature were set up. The models were ran in an adiabatic manner, thus heat transfer effects

were neglected and only the mechanical response calculated, and the pipe assumed to remain at the same fixed temperature (either 15°C to represent a cold fluid carrying pipe, and 80°C to represent a hot fluid carrying pipe). This was considered a fair simplification given the pipe will remain at the temperature of the fluid carried during the pipe collapsing procedure, with additional heating due to deformation minimal and thus neglected.

A normalised Cockroft and Latham damage criterion was implemented within the plastically deforming workpiece to simulate the potential for fracture at regions of high strain and stress, to keep a through process track of the evolution of this damage parameter indicating the material likelihood to fracture. The normalised Cockroft and Latham parameter, C_n, is expressed as given in Equation 2.

$$C_n = \int^{\bar{\epsilon}} \frac{\sigma_{max}}{\sigma_{eff}} d\bar{\epsilon_p} \qquad (2)$$

Whereby; σ_{max} is the maximum principal stress, σ_{eff} is the effective (Von Mises) stress, and $\bar{\epsilon_p}$ is the effective plastic strain. The normalising parameter in this equation is the effective stress, and this allows for a fracture likelihood parameter, Cn, to be postulated. No value was set to initiate element deletion; instead the model was allowed to simply accrue damage at locations of likely high stress and strain to give an idea of probable damage sites within the workpiece.

4 Results and Discussion

4.1 Shape

The resulting deformed pipe cross-sectional shapes at different applied loads, predicted using FE software, were critically compared to the experimentally observed pipe cross-sectional shape, to determine the accuracy of the modelling approach. The resulting pipe cross-sections for the cold pipe can be seen in Figure 3(A),3(B).

In the experiment (see Figure 3(B)), the pipe is deforming reasonably consistently with an elliptical mode. At the 2.5 kN load, a "flat" section appears on the top and bottom surfaces, where the apex location had been before. At higher loads, this flat actually turns inward, such that the location along the vertical centre of the pipe will come in to contact first. This central contact is achieved at the 6 kN load experiment, whereby the pipe has collapsed on to itself along its vertical centre-line. Thus, in the experiment, the elliptical mode of deformation is a reasonable approximation up until a force of greater than 3 kN.

For the FE model, the inverting of the pipe wall at the

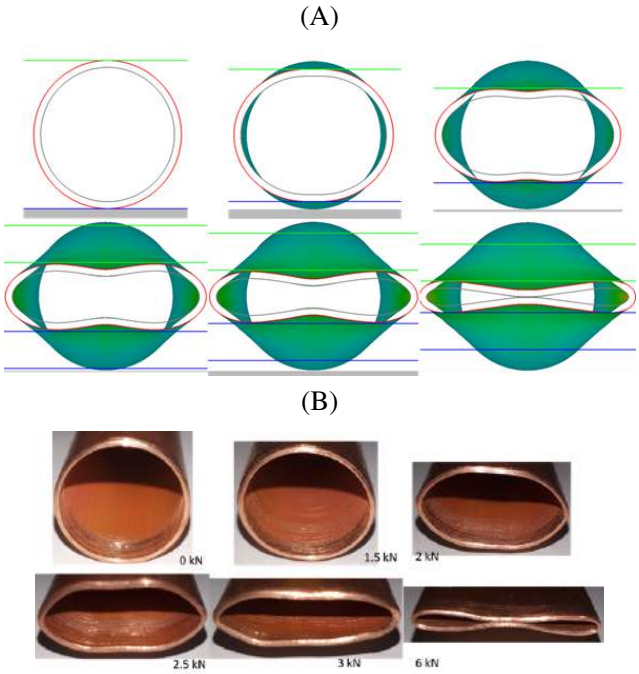

Figure 3. **(A)** Shape predictions for the cold (15°C) pipe at: (1) un-deformed; (2) 1.5kN; (3) 2kN; (4) 2.5kN; (5) 3kN; (6) 6kN **(B)** Experimentally observed pipe deformation shapes at: (1) un-deformed; (2) 1.5kN; (3) 2kN; (4) 2.5kN; (5) 3kN; (6) 6kN

vertical apex locations, such that they turn in toward one another, is predicted to occur at a lower applied load. This is manifested within the 2.5 kN load model, and then continues to become more pronounced until contact is reached, somewhere in between the 3 kN and 6 kN loads. Whilst the applied load at which this first begins is not in agreement with the experiment, the overall trend is correctly predicted. However, it must be stressed that for the FE model, the elliptical deformation mode has broken down for much of the deformation.

The FE modelling framework was extended to also consider the deformation of the same set-up of FE model, but considering a pipe held at a heated 80°C (see Figure 4). This is performed in order to simulate the deformation experienced upon a hot water carrying pipe, where the copper material will have a slightly different mechanical response than when cold (15°C). Again, the trend is shown for an initial elliptical deformation mode to give way to a deformation mode whereby the upper and lower apex locations "turn-in" to produce a slightly narrowed section at the vertical centreline of the pipe.

4.2 Force

The FE model can be interrogated to generate a force vs die separation plot, to predict the collapse pf the pipe under increasing applied loads. The die separation, by definition of the problem, is simply the "height" of the

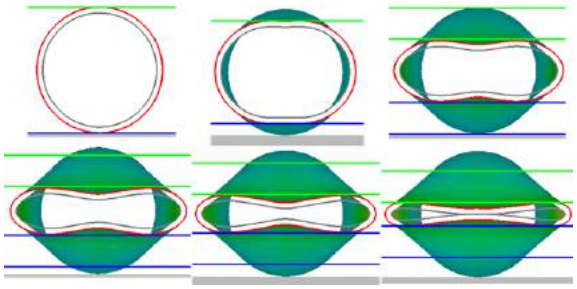

Figure 4. Shape predictions for heated (85°C) pipe at: (1) undeformed; (2) 1.5kN; (3) 2kN; (4) 2.5kN; (5) 3kN; (6) 6kN

deforming pipe in the vertical axis, in-between the tooling applying the loading. The predicted die separation for a given applied force, for the models simulating a cold fluid carrying pipe at 15°C, and for simulating a heated fluid carrying pipe at 80°C can be seen in Figure 5.

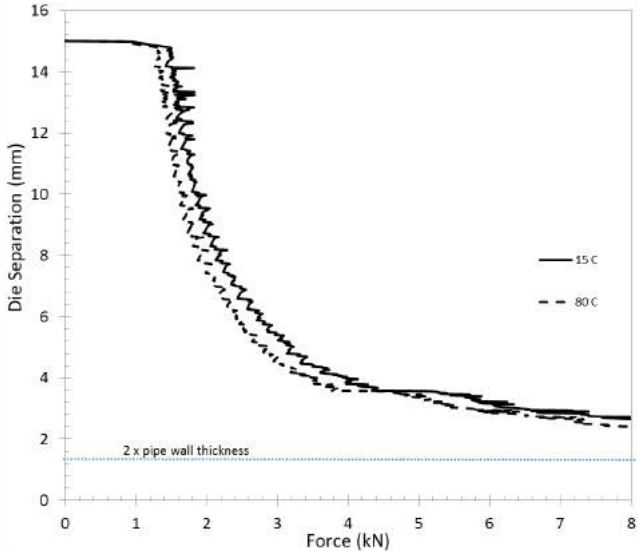

Figure 5. Die separation versus corresponding applied force graph, to illustrate the gradual collapse of the pipe

The onset of deformation of the pipe can be seen to occur for the cold pipe at approximately 1.5 kN, whereas for the heated pipe, this deformation initiates at approximately 1.25 kN. Thus, there is evidently some flow softening of the copper at 80°C compared to 15°C, given that for the same applied load the pipe is deformed more, hence the two dies are closer together.

The resulting semi-minor axis length of the pipe (which by definition is half of the die separation value, measured vertically in the set-up) continues to decrease approximately linearly between 1.5 kN and 2 kN (for the cold pipe) or between 1.25 kN and 1.75 kN (for the 80°C heated pipe), when the reduction in semi-minor axis begin to slow down. As the pipe becomes more plastically distorted, increasing applied loads continue to increase deformation within the pipe, but to a smaller effect, as the deformation approaches a natural asymptote, namely the thickness of two pipe walls for when the pipe has entirely flattened out upon itself, which it cannot be compressed more than.

The pipe deforms initially following the elliptical pipe-wall shape, as shown previously. However, at an applied load of 2 kN, the apex of the upper and lower wall of pipe begin to turn inwards, thus the elliptical description breaks down slightly from this moment onwards. An applied load of 6 kN for the cold pipe model sees these apex positions of upper and lower wall meet. For the heated pipe, this contact of pipe walls occurs at a marginally lower applied force, 5.5 kN. Once the walls contact, the semi-minor axis value (still assuming that one can use an ellipse to describe the pipe, which is not strictly true) decreases a small amount for greater and greater loads, as the pipe is now flattening on to itself.

4.3 Residual stress

The structural integrity of the copper pipe will predominantly depend upon the levels of residual stresses experienced and associated strain within the component, as it is crushed and deformed. It is therefore of interest to be able to analyse these *in-situ* fields of strain and effective (Von Mises) stress across the component during deformation. This capability to perform detailed through-process interrogation of mechanical fields is the primary strength of any FE analysis, if it is assumed that the model has been successfully validated by comparison of shape prediction against experimentally observed deformed pipe shape. Instrumented experimentation to understand the temporally through-process stress and strain fields is extremely challenging, hence the ability to analyse with validated FE tools is a convenient way of understanding how the deformation process influences these mechanical fields.

The Von Mises stress field within the pipe, during differing loads considered, can be seen in Figure 6. Peak Von Mises stresses for the models at the applied loads range from 240 MPa in the 1.5 kN model to 440 MPa in the 6kN model for the cold pipe, and from 240 MPa in the 1.5 kN model to 380 MPa in the 6 kN model for the heated pipe. Whilst the peak stresses did fall approximately 15% in the heated pipe model, it was the difference in Von Mises stress across the central portion of the pipe that saw the greatest decrease when the pipe was heated. At the 6 kN applied force, the modal Von Mises stress value reported at nodes was 250-260 MPa for the cold pipe, whereas it was only 210-220 MPa for the heated pipe, thus the lower banding of predominant

colour in the heated pipe model (see Figure 6).

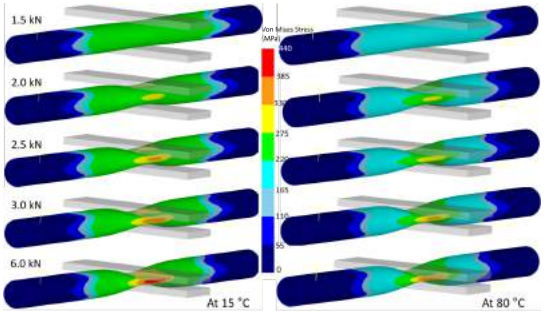

Figure 6. Von Mises residual stress after pipe crushing, at the 5 varying applied loads, for (left) cold 15°C pipe, and (right) heated 80°C pipe

Clearly, the region under the highest stress will be the "shoulder" region of the deformed section of pipe, where the pipe wall is being pushed outward perpendicular to the applied force. However, Von Mises stress does not distinguish between compressive and tensile values. The nature of the stress field can be further interrogated by considering the stress field in the vertical direction (direction of applied load), see Figure 7. For the cold pipe 6 kN applied load model, the pipe cross-section in the X-Z plane through the region of maximum Von Mises stress was analysed.

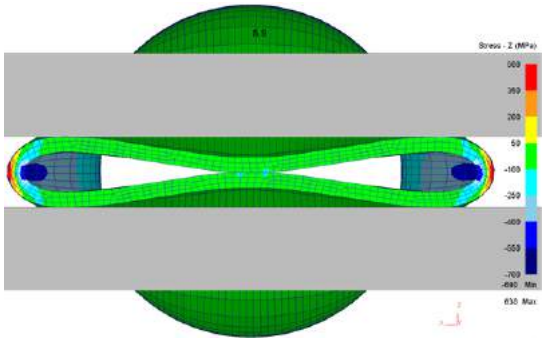

Figure 7. Von Mises residual stress, shown over a cross-section of cold (15°C) pipe for the 6 kN load

The shoulder region experiencing the maximum stress is under a tensile stress field on the outer wall of the pipe, as it is perpendicular to the applied force, whereas the top and bottom of the pipe will experience a compressive stress given these are in the axis of deformation. However, the inner wall, at the location of maximum displacement, must in turn experience a compressive stress, to balance the tensile stress elsewhere. For this highest applied load model (6 kN), the tensile stress in the Z direction on the outer wall reaches similar values to that given by the Von Mises effective stress, approximately 450 MPa, as this is by far the largest contributor in terms of the principal stress axes at this location., thus dominates the equation to calculate Von Mises stress from the principal stress fields. The inner wall sees compressive stresses of a similar magnitude, approximately 470-500 MPa. These predicted peak tensile and compressive stresses fall for the lower applied loads, to approximately 240 MPa (tensile outer wall and compressive inner wall) for the lowest applied load (1.5 kN) for which there is minimal distortion.

4.4 Effective strain

The FE model predicted effective strain fields experienced within the cold and the heated deformed pipe, at the different applied loads, are given in Figure 8. As with the effective stress field, it is clear that the maximum strain will be observed at the shoulder region where the applied load is acting, as this must deform more than any other region in the pipe. The peak effective strain predicted for the models ranges from less than 0.05 for the 1.5 kN applied load, to 0.4 for the 6 kN load. The peak effective strain increases roughly linearly proportionally to the applied load across the 5 models, with an approximate empirically fitted relationship of $\epsilon_{max} = \frac{F\ (kN)}{20}$.

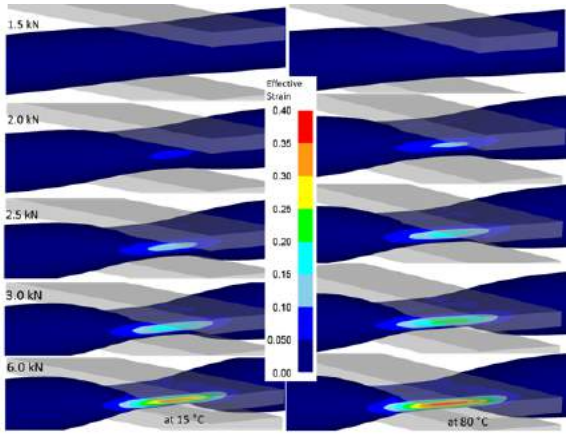

Figure 8. Effective strain for pipes at the 5 varying applied loads; (left) cold 15°C pipe, and (right) heated 80°C pipe

The effective strain field, viewed at the cross-section of the pipe in the X-Z plane, through the point of maximum strain, was analysed. Figure 9 illustrates this cross-sectional view for the 6 kN applied load model, and it is evident that within the predicted strain field, the strain is highest on both the outer and inner walls at the horizontal apex location. Peak effective strain values for the 6 kN applied load are reaching approximately 0 35 on the inner wall, and 0.3 on the outer wall in this plane. The strain reduces to a minimum of roughly half the peak value, at approximately half-way through the 0.7 mm

thick wall.

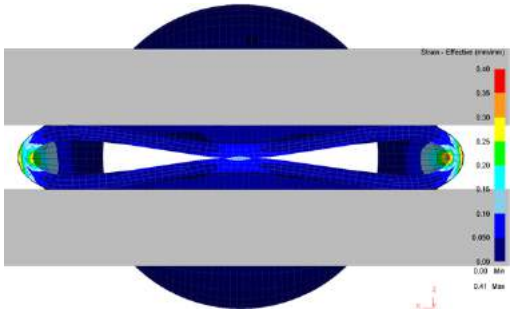

Figure 9. Effective strain, shown over a vertical cross-section of pipe at maximum distortion, for the 6 kN load

4.5 Fracture / Damage

The FE model can be interrogated to determine the level of "damage" accumulation throughout the pipe, according to the Cockroft and Latham normalised parameter, as defined previously. The maximum accumulation of damage, unsurprisingly given the mathematical description of the parameter, occurs at the outer wall, at the horizontal apex location where the pipe is forming a corner as it begins to fold on to itself.

Figure 10 compares this FE predicted damage parameter against the experimentally observed damage at the same specific location on the pipe which was noted for having peak damage parameter values. Observe that the location of damage observed matches very well with the predicted peak damage in the FE modelling framework. It is therefore considered as further validation of both the damage parameter estimation, and the modelling framework as a whole, that a pure prediction made by modelling has been well-matched against physically observed evidence.

The models were further interrogated to attempt to construct a value for the threshold of normalised Cockroft and Latham damage which will lead to onset of cracking damage within the copper. By considering experimentally observed damage was accumulated somewhere in between the 3 kN and 6 kN applied load, so consultation of these FE models, at the relevant location, suggests a normalised Cockroft and Latham parameter of between 0.25 and 0.35 was the trigger value for the onset of damage.

5 Flow, pressure drop and head loss theory

In order to assess the fitness for purpose of these pipes after suffering the level of deformation experimentally observed and predicted by FE analysis, one must consider the fundamental fluid mechanics, pipe flow, pressure loss and corresponding head loss governing equations. The flow of the fluid being carried by the pipe will depend upon a number of parameters, some associated with the fluid, and some associated with the pipe. As the fluid parameters will be dependent upon temperature, these calculations are performed for both a cold water scenario (15°C) and a hot water scenario (80°C). These calculations are initially performed for the nominal undamaged copper pipe (with perfect circular cross-section), as well as for the 5 examples of deformed pipe cross-sections, as simulated and discussed earlier, for 5 differing loads applied.

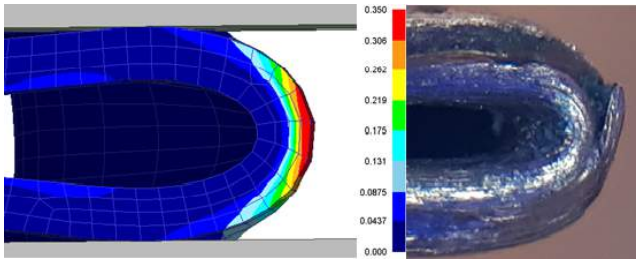

Figure 10. The normalised Cockroft and Latham damage parameter used in the FE model shown as a displayed field over the workpiece, compared to the experimentally observed location of damage

One can calculate the relative pipe roughness of the copper pipe using Equation 3, where ϵ is the characteristic surface roughness of copper (estimated to be 0.03 mm), and d the pipe diameter[25] .

$$R = \frac{\epsilon}{d} \tag{3}$$

By making the assumption that the fluid is incompressible, thus we must assume a volumetric flow rate Q is conserved through the process, whereby, for a volumetric flow rate Q, fluid average velocity v and pipe cross section A, the following relationship (Equation 4) holds

$$Q = Av \tag{4}$$

As A will change as the pipe is being deformed, so therefore must v change, to maintain a constant Q. One can calculate the cross-sectional area, assuming that the deformed pipe is represented by a perfect elliptical deformed pipe wall, thus one can calculate v. Note the assumption here that the pipe is deforming as an ellipse, which is a good approximation for lower applied loads to deform, although becomes a worse fit at higher loads. Therefore, one can similarly calculate the Reynolds value of the water flowing in the pipe, using Equation 5[26] .

$$Re = \frac{\rho v d}{\mu} \tag{5}$$

Where ρ is the density of water, v is the flow velocity of the water, and μ is the dynamic viscosity. With calculated values for both the Reynolds value of the moving fluid, and the relative pipe roughness coefficient, the Moody chart can be consulted to understand the Darcy friction factor term of the pipe wall, f_D, as it impedes the flow of the water.

However, when considering the deformed pipe, one must adapt the simplistic formulae, as this is no longer the simple circular cross-section pipe case. In order to calculate relevant properties of the deformed pipe, we will need characteristic dimensions of this non-circular pipe. If we assume the deformed pipe has an elliptical cross section, with a semi-major axis r_α and semi-minor axis r_β, then by using the Ramanujan approximation[27] (Equation 6) we can calculate the pipe circumference.

$$C = \pi \left[3\left(r_\alpha + r_\beta\right) - \sqrt{10 r_\alpha r_\beta + 3\left({r_\alpha}^2 + {r_\beta}^2\right)} \right] \tag{6}$$

In order to calculate the Reynolds value and the relative pipe roughness we require a pipe diameter to be known. In the case of a deformed pipe, we will apply the hydraulic diameter d_H, which is defined in Equation 7[28] :

$$d_H = 4\frac{Area}{wetted\ circumference} = 4\frac{\pi r_\alpha r_\beta}{C} \tag{7}$$

We must then use the hydraulic diameter d_H in place of the diameter d in the equations for effective pipe roughness, pressure drop and head loss. These equations also depend upon the Darcy term f_D, to calculate the pressure drop caused by the frictional resistance of the pipe wall, over a given length (L) of pipe, or to calculate the effective head loss, again over a given length, using Equation 8 and Equation 9[26] , where g is the gravitational acceleration.

$$\frac{\Delta P}{L} = f_D \frac{1}{d_H}\frac{\rho v^2}{2} \tag{8}$$

$$\frac{h_{loss}}{L} = f_D \frac{1}{d_H}\frac{v^2}{2g} \tag{9}$$

The resulting effective circumference, hydraulic diameter, relative pipe roughness, flow velocity, Reynolds value, Darcy friction factor pressure drop and the equivalent head loss values for the pipe as it has undergone different applied loads to deform it can be compared to nominally un-deformed pipe, these values are given in Table 2 and Table 3. For the calculations performed as part of this work, the pipe length is assumed to be 1 metre, thus all expressed pressure drops and equivalent head losses are per metre of damaged, crushed pipe.

The following values are used for cold (15°C) and heated (80°C) water as the fluid of interest. For 15°C water, density ρ = 1000 kgm^{-3}[29] , dynamic viscosity μ = 8.9 x 10^{-4} Pa.s[30] , and the maximum suggested flow velocity for cold water in a non-deformed pipe is 2.4 ms^{-1}, which gives a constant volumetric flow for a 15 mm diameter circular pipe of 0.424 x 10^{-3} m^{3}s^{-1}. For 80°C water, density ρ = 970 kgm^{-3}[29] , dynamic viscosity μ = 3.5 x 10^{-4} Pa.s,[30] and the maximum suggested flow velocity for cold water in a non-deformed pipe is 1.5 ms^{-1}, which gives a constant volumetric flow for a 15mm diameter circular pipe of 0.265 x 10^{-3} m^{3}s^{-1}. The assumed elliptical pipe sections used from the experiment and FE models at different deforming loads were illustrated in Figure 3 and Figure 4.

A cold-fluid carrying pipe, with the fluid and pipe wall held at 15°C (see Table 2), would see the fluid flow velocity increase slightly as the deformation began, as the interior cross-section of the pipe was beginning to reduce, so the flow velocity increases to maintain the constant volumetric flow rate. As the deformation continued and the interior cross-sectional area of the pipe became smaller still, the flow velocity does begin to increase substantially. However, the Reynolds number for the flow remains virtually constant, because it is a function of both the flow velocity and the characteristic distance, namely the pipe hydraulic diameter, which is reducing.

The Darcy friction factor, which is determined using the Moody diagram, remains relativity constant until the pipe relative roughness increases substantially. This increase is in turn caused by the hydraulic diameter reducing significantly to less than half its starting value. It then increases slightly for the highly deformed pipe. Thus, the pressure loss per unit length of pipe, and the corresponding head loss per unit length of distorted pipe, can be calculated. As the pressure loss per unit length of pipe is a function of the Darcy friction factor, the flow velocity squared, and inversely proportional to the hydraulic diameter, so all terms are working to increase the pressure as the pipe becomes more and more deformed. The pressure loss per unit length of pipe for an applied load of 2 kN increases to approximately double the pressure loss for an un-deformed pipe. The pressure loss continues to increase rapidly, becoming severe at a 2.5 kN applied load, and is catastrophic at 6 kN applied load. Similarly, the head loss per unit length of pipe increases such that it is approximately double that of the un-deformed pipe when a 2 kN load is applied, but this head loss increases rapidly for even higher applied loads.

Table 2. Theoretically calculated pipe flow characteristics for the cold 15°C pipe, from first principles

At 15℃	Un-deformed	Deforming Load (kN)				
Pipe / Flow Property	**0**	**1.5**	**2**	**2.5**	**3**	**6**
Semi-major axis (mm)	6.8	7.4	8.6	9.3	9.7	10.2
Semi-minor axis (mm)	6.8	6.0	4.1	2.7	2.0	0.9
Ramanujan Circumference (mm)	42.7	42.0	41.2	40.7	40.9	41.2
Hydraulic diameter (mm)	13.6	13.2	10.8	7.8	5.8	2.8
Relative pipe roughness (-)	0.0022	0.0023	0.0027	0.0038	0.0050	0.0100
Fluid velocity (m/s)	2.9	3.1	3.8	5.4	7.1	14.7
Reynolds value (-)	44,500	45,300	46,200	46,800	46,500	46,100
Darcy friction factor (-)	0.028	0.028	0.028	0.029	0.033	0.040
ΔP (per 1m pipe) (kPa)	8.76	9.97	18.80	53.50	142.40	1545.60
h_{loss} (per 1m pipe) (m)	0.89	1.01	1.91	5.46	14.50	157.80

However, given that the damage caused to a pipe through some type of pinching or crushing action is usually across a narrow section of pipe, almost giving rise to point-damage due to the impact of an external object, so the actual length of the deformed section of pipe is likely very short, of the order of a few centimetres in length, thus the actual pressure drop and head loss over the deformed length of pipe is likely scaled accordingly.

Similar trends are shown for the heated pipe (see Table 3), in that the method of shaping the deformed pipe is very similar to the cold pipe, albeit the distortions are slightly larger for a given applied load, due to the small reduction in flow stresses at this elevated temperature, compared to cold. The hydraulic diameter, calculated from the semi-major and semi-minor lengths, decreases considerably once a load greater than approximately 1.5 kN is applied. As for the cold pipe, it is the significant decrease in hydraulic diameter, which is proportional to the relative roughness term, which causes the major changes in the Darcy friction factor calculation, which increases by roughly a third from the un-deformed pipe value. However, again as with the cold pipe, the fluid flow velocity increase is the critical parameter which dictates the catastrophic pressure and head loss per unit length of deformed pipe.

Figure 11 illustrates the changes calculated in the hydraulic diameter of the pipe, and the resulting pressure drop per unit length of pipe, from the theoretical hand calculations based upon fluid flow within a contained pipe, for different deforming loads applied to the pipe, and at the two different fluid and pipe temperatures. Figure 11 illustrates clearly the beginning of severe reduction in hydraulic diameter as the pipe is deforming, as the theoretically calculated hydraulic diameter suffers a cliff-edge drop off in between 1.5 and 2 kN applied load. Figure 11 illustrates the theoretically calculated increase in pressure drop for increasing deforming load applied to the pipe. This graph is clearly dominated by the relationship with the velocity squared, such that for the relatively linear increase seen in fluid velocity when increasing the applied load from 1.5 kN upwards, the pressure drop increases with a $y=f(x^2)$ type response.

6 Conclusions

A finite element modelling framework has been presented to predict the deformation of 15 mm outer diameter, 0.7 mm wall thickness copper pipes, with tooling

Table 3. Theoretically calculated pipe flow characteristics for the hot 80°C pipe, from first principles

At 80℃	Un-deformed	Deforming Load (kN)				
Pipe / Flow Property	0	1.5	2	2.5	3	6
Semi-major axis (mm)	6.8	7.8	9.3	9.7	10.0	10.3
Semi-minor axis (mm)	6.8	5.4	2.9	2.0	1.6	0.9
Ramanujan Circumference (mm)	42.7	41.8	41.2	41.0	41.3	41.8
Hydraulic diameter (mm)	13.6	13.2	8.3	6.0	4.7	2.6
Relative pipe roughness (-)	0.0022	0.0024	0.0036	0.0050	0.0063	0.0110
Fluid velocity (m/s)	1.8	2	3.1	4.3	5.4	9.6
Reynolds value (-)	68,800	70,200	71,300	71,500	71,100	70,200
Darcy friction factor (-)	0.027	0.027	0.028	0.030	0.032	0.039
ΔP (per 1m pipe) (kPa)	3.20	4.20	15.30	45.60	97.40	660.00
h_{loss} (per 1m pipe) (m)	0.34	0.44	1.61	4.79	10.25	69.15

acting under to apply particular loads to pinch or trap the pipe. Experimental pipe crushing trials were undertaken to validate the modelling approach. In addition, theoretical pipe flow characteristics of the deformed pipes, under different loads, at two different temperatures have been calculated. The following conclusions are drawn:

(1) For cold pipes, an applied force of 1.5 kN will cause an onset of deformation, causing the pipe to begin to become elliptical. The pipe approaches a state of collapse, whereby the upper wall contacts the lower wall, and thus a catastrophic loss of integrity, at an applied load of 6 kN.

(2) Whereas for pipes at 80°C, an applied force of 1.25 kN causes the onset of plastic deformation. However, the reduction in required force compared to the cold pipe remains at approximately the same value of $\frac{1}{4}$ kN lower, thus the heated pipe requires approximately $5\frac{1}{2}$ to $5\frac{3}{4}$ kN deforming load to achieve the same form of collapse as seen in the cold pipe.

(3) The flow of fluid through the piping remains at approximately the same Reynolds value throughout. However, as the pipe deforms, the hydraulic diameter reduces, the required flow velocity increases, and as such the pressure loss per unit length of pipe, and head loss per unit length, increase with a $y = f\,(x^2)$ type response.

(4) The elliptical deformation of the pipes holds reasonably true until a deforming load of 2kN, whereby the top and bottom apex inversion within the deforming pipe becomes substantial compared to the semi-minor axis.

(5) The normalised Cockroft and Latham damage parameter predicted with reasonable accuracy the location of damage observed experimentally on the copper pipe, and an approximate value to initiate macro-scale damage has been estimated as 0.25-0.35.

Acknowledgements

Thanks are offered to the technical support staff at Wilde Analysis, Stockport, UK, for their technical assistance with the FE modelling. Thanks are offered to David Price, in the mechanical testing laboratory, School of Metallurgy & Materials, University of Birmingham.

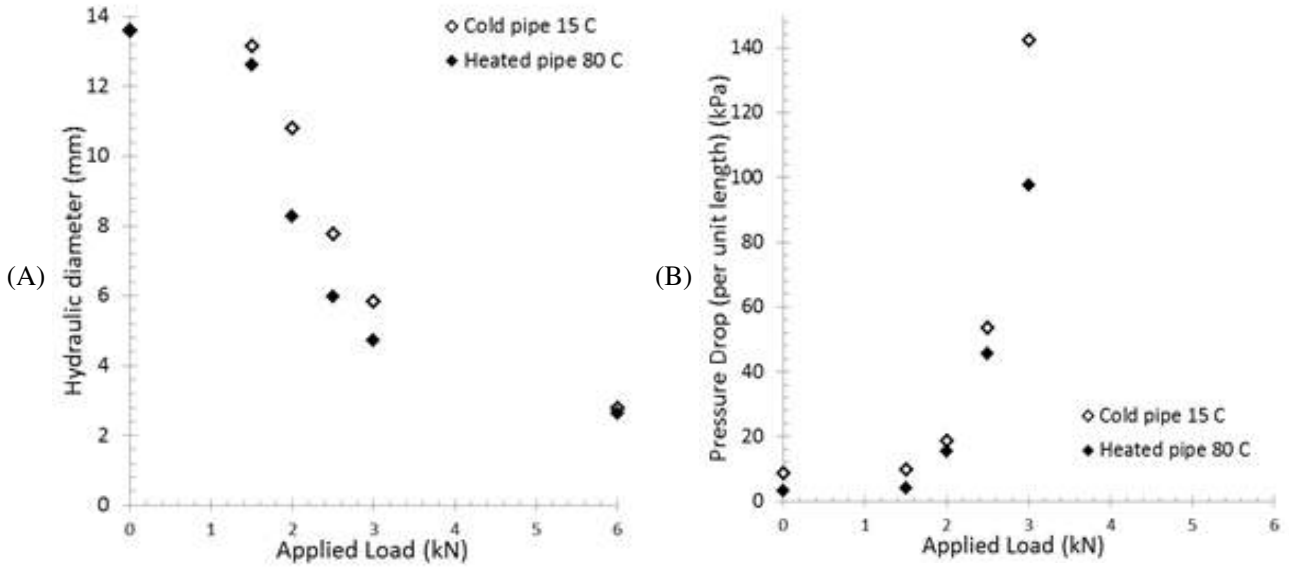

Figure 11. **(A)** graph showing the theoretically calculated hydraulic diameter, and **(B)** graph showing the theoretically calculated Pressure drop, for differing applied loads

References

[1] Petersen Products Co., 421 Wheeler Ave, Fredonia, WI 53021-0340, US, 2017.

[2] Copper Development Association Inc.

[3] Canadian Copper and Brass Development Association, Toronto, M4H 1P1, Canada, 2019.

[4] Dick RJ, Wray JA and Johnston HN. A Literature and Technology Search on the Bacteriostatic and Sanitizing Properties of Copper and Copper Alloy Surfaces, Phase 1 Final Report, INCRA Project No. 212, June 29, 1973, contracted to Battelle Columbus Laboratories, Columbus, Ohio.

[5] Minnesota Department of Health, 625 North Robert Street, St Paul, Minnesota.

[6] Wednesbury Copper Tube, Mueller Europe Ltd, Oxford Street, Bilston, WV14 7DS, UK.

[7] Fateh A, Aliofkhazraei M and Rezvanian AR. Review of corrosive environments for copper and its corrosion inhibitors. Arabian journal of Chemistry, In press, 2017. https://doi.org/10.1016/j.arabjc.2017.05.021

[8] Materials Data Handbook, Cambridge University Engineering Department, UK, 2003 Edition, 13.

[9] Dubreuil A, Young SB, Atherton J, *et al*. Metals recycling maps and allocation procedures in life cycle assessment. The International Journal of Life Cycle Assessment, 2010, **15**(6): 621-634. https://doi.org/10.1007/s11367-010-0174-5

[10] Amos J. Waste and Recycling. Heinemann Raintree, 1993.

[11] ASM Metal Recycling, The Recycling Centre, Aylesbury, Bucks, HP19 8BB, UK.

[12] Kundig KJA. Copper Applications in plumbing. Copper Development Association, 1998.

[13] Miller R. Making Seamless tubing with a floating mandrel mill. Tube and Pipe Journal, 2000.

[14] Chapman DSC. Effect of process variables on the tube drawing process and product integrity, Master's Thesis, Texas Tech University, USA, 1991.

[15] DeGarmo EP, Black JT and Kohser RA. Materials and Processes in Manufacturing, Wiley, 2003.

[16] Lide DR. CRC Handbook of Chemistry and Physics. 84th Edition, CRC Press, Florida, USA, 2004.

[17] Katsareas DE. Finite Element Simulation of Welding in Pipes: A sensitivity analysis. Residual stress and its effect of fracture, Springer, Dordrecht, 2006: 15-26. https://doi.org/10.1007/1-4020-5329-0_2

[18] Yaghi A, Hyde TH, Becker AA, *et al*. Residual stress simulation in thin and thick-walled stainless steel pipe welds including pipe diameter effects. The International Journal of Pressure Vessels and Piping, 2006, **83**(11-12): 864-874. https://doi.org/10.1016/j.ijpvp.2006.08.014

[19] Yaghi AH, Hyde TH, Becker AA, *et al*. Finite element simulation of welding residual stresses in martensitic steel pipes. Materials Research Innovations, 2013, **17**(5): 306-311. https://doi.org/10.1179/1433075X13Y.0000000140

[20] Zhou Y, Chen XD, Fan ZC, *et al*. Finite Element Modelling of Welding Residual Stress and Its Influence on Creep Behavior of a 2.25Cr-1Mo-0.25V Steel Cylinder. Procedia Engineering, 2015, **130**: 552-559. https://doi.org/10.1016/j.proeng.2015.12.264

[21] Siddique M, Abid M, Junejo HF, *et al*. 3-D Finite Element Simulation of Welding Residual Stresses in Pipe-Flange Joints: Effect of Welding Parameters. Materials Science Forum, 2005, **490-491**: 79-84. https://doi.org/10.4028/www.scientific.net/MSF.490-491.79

[22] Mohammad R. Impact loading and transient response of pipes transporting gas / liquid, University of Adelaide. PhD Thesis, 2011.

[23] Kwan A, Ng PL and Lam JY. Potential underground pipe failure due to load concentration at pipe crossings, The First International Conference on Utility Management and Safety, Hong Kong, China, 2009.

[24] Scientific Forming Technologies Corporation, 2545 Farmers Drive, Columbus, Ohio 43235, USA.

[25] Moody L. Friction Factors for pipe flow. Transactions of the ASME, 1944, **66**(8): 671-684.

[26] Acheson DJ. (1990), Elementary Fluid Dynamics, Oxford University Press, Oxford, UK, 1990.

[27] Ramanujan S . Modular equations and approximations to π. Also in Collected Papers of Srinivasa Ramanujan, Gh Hardy, Pv Seshu Aiyar, & Bm. 1914. https://doi.org/10.1007/978-1-4757-4217-6_29

[28] White FM. Fluid Mechanics (7^{th} Ed.), MacGraw-Hill Asia, 2011.

[29] Greenwood NN and Earnshaw A. Chemistry of the Elements (2^{nd} Ed.), Butterworth-Heinemann, 1997.

[30] Rumble JR. CRC Handbook of Chemistry and Physics (99^{th} Ed.). Boca Raton, FL: CRC Press, 2018

Materials Engineering Research an independent open access journal published by Syncsci Publishing. Pte. Ltd.

Syncsci Publishing. Pte. Ltd.
50 Chin Swee Road
#09-04 Thong Chai Bldg
Singapore 169874
Tel : (+65) 68264112; (+65)98107233
Email : editorial@syncsci.com
Website: www.syncsci.com

Print Version USD 75.00